

# GLOBAL MECHANICAL RESPONSE AND ITS RELATION TO DEFORMATION AND FAILURE MODES AT VARIOUS LENGTH SCALES UNDER SHOCK IMPACT IN ALUMINA AD995 ARMOR CERAMIC

D. P. Dandekar\*, J. W. McCauley, and W. H. Green  
Army Research Laboratory, APG, MD 21005

N. K. Bourne  
University of Manchester, UK

M. W. Chen  
Johns Hopkins University, Baltimore MD and Tohoku University, Sendai, Japan

## ABSTRACT

Polycrystalline aluminum oxide ( $\text{Al}_2\text{O}_3$ ) based materials have both personnel and ground vehicle armor applications. However, as their ballistic performance can vary significantly it is important to identify the fundamental macro and micro mechanisms of deformation and failure in the ballistic event. This has proven elusive over the years. Using a newly developed soft recovery plate impact experiment, a multi-disciplinary, multi-national collaboration has, for the first time, determined micro and macro deformation and damage mechanism maps relating the experimentally measured global mechanical response of a material through matured shock wave diagnostics to the nature of concurrent deformation and damage generated at varying length scales under shock wave loading.

## 1. INTRODUCTION

Current operations in Iraq and Afghanistan unambiguously demonstrate the need for threat specific, reduced weight, transparent and opaque armor in many army systems, including personnel protection. As the threats have escalated and become more varied, the challenges for rapidly developing optimized threat specific armor packages have grown complex. Certain high performance structural ceramics,  $\text{Al}_2\text{O}_3$ ,  $\text{B}_4\text{C}$ ,  $\text{SiC}$ ,  $\text{TiB}_2$ ,  $\text{AlN}$ ,  $\text{AlON}$ , spinel, glass, etc. have proven to be effective armor materials at much lower weights in many systems. A critical key to further accelerating optimization of these materials is development of validated predictive performance computer models. This approach is based on the determination and quantification of the various ballistic energy absorption mechanisms, including the various deformation modes, damage nucleation and accumulation processes, and the resulting eventual failure of armor ceramics at high rates under very high impact stress (shock wave), comparable to the ballistic event.

Polycrystalline aluminum oxide ( $\text{Al}_2\text{O}_3$  - alumina), known as sapphire in single crystal form, has been used for many years in both personnel and ground vehicle armor applications. Yet the ballistic performance of alumina based armor ceramic materials can vary significantly, a major challenge for systematic material optimization, valid simulation, prediction, and design of armor systems. We seek to address this problem through identification of the fundamental mechanisms of deformation and failure of alumina in the ballistic event.

Past efforts have used instrumented laboratory high strain rate/high pressure mechanical tests including Split Hopkinson Pressure Bar (SHPB/ Kolsky Bar) and plate impact (shock wave) to mimic, in a controlled environment, the response of armor materials under ballistic high strain rate – high stress conditions. But there are two major problems associated with this approach: (A) recovery of samples from the test suitable for detailed characterization, and (B) identification of the deformation and failure mechanisms that cut across length scales from centimeters to nanometers. This has been a major challenge over the years.

Using a newly developed soft recovery technique (Bourne et. al. 2006), an international team drawn from the Army Research Laboratory (ARL), Royal Military College of Science (RMCS), Shrivenham, UK, the University of Manchester, Manchester, UK, Johns Hopkins University and Tohoku University, Sendai, Japan, focused on AD995 (CoorsTek, Co.), a very well known commercial high purity alumina. This collaboration has, for the first time, determined micro and macro deformation and damage mechanism maps that relate the experimentally measured global mechanical response of a material through matured shock wave diagnostics to the nature of concurrent deformation and damage generated at varying scales under shock wave loading. These results can provide a critical missing link in the development of better physical material models and materials.

## 2. MATERIAL

# Report Documentation Page

*Form Approved*  
*OMB No. 0704-0188*

Public reporting burden for the collection of information is estimated to average 1 hour per response, including the time for reviewing instructions, searching existing data sources, gathering and maintaining the data needed, and completing and reviewing the collection of information. Send comments regarding this burden estimate or any other aspect of this collection of information, including suggestions for reducing this burden, to Washington Headquarters Services, Directorate for Information Operations and Reports, 1215 Jefferson Davis Highway, Suite 1204, Arlington VA 22202-4302. Respondents should be aware that notwithstanding any other provision of law, no person shall be subject to a penalty for failing to comply with a collection of information if it does not display a currently valid OMB control number.

1. REPORT DATE <b>01 NOV 2006</b>	2. REPORT TYPE <b>N/A</b>	3. DATES COVERED -			
4. TITLE AND SUBTITLE <b>Global Mechanical Response and its Relation to Deformation and Failure Modes at Various Length Scales under Shock Impact in Alumina AD995 Armor Ceramic</b>		5a. CONTRACT NUMBER			
		5b. GRANT NUMBER			
		5c. PROGRAM ELEMENT NUMBER			
6. AUTHOR(S)		5d. PROJECT NUMBER			
		5e. TASK NUMBER			
		5f. WORK UNIT NUMBER			
7. PERFORMING ORGANIZATION NAME(S) AND ADDRESS(ES) <b>Army Research Laboratory, APG, MD 21005</b>		8. PERFORMING ORGANIZATION REPORT NUMBER			
9. SPONSORING/MONITORING AGENCY NAME(S) AND ADDRESS(ES)		10. SPONSOR/MONITOR'S ACRONYM(S)			
		11. SPONSOR/MONITOR'S REPORT NUMBER(S)			
12. DISTRIBUTION/AVAILABILITY STATEMENT <b>Approved for public release, distribution unlimited</b>					
13. SUPPLEMENTARY NOTES <b>See also ADM002075., The original document contains color images.</b>					
14. ABSTRACT					
15. SUBJECT TERMS					
16. SECURITY CLASSIFICATION OF:			17. LIMITATION OF ABSTRACT  <b>UU</b>	18. NUMBER OF PAGES  <b>39</b>	19a. NAME OF RESPONSIBLE PERSON
a. REPORT <b>unclassified</b>	b. ABSTRACT <b>unclassified</b>	c. THIS PAGE <b>unclassified</b>			

AD995 is composed of polycrystalline aluminum oxide ( $\text{Al}_2\text{O}_3$ ) and aluminosilicate glass. It contains 99.5% aluminum oxide. The measured density of AD995 is  $3.880 \pm 0.003 \text{ Mg/m}^3$ . Theoretical density of such a material should be  $3.96 \text{ Mg/m}^3$ . The difference is attributed to the presence of a glassy phase and pores/voids in the material [Figure 1]. Ultrasonic longitudinal and shear wave velocities are  $10.56 \pm 0.03$ , and  $6.25 \pm 0.08 \text{ km/s}$ , respectively (Dandekar and Bartkowski 1994).

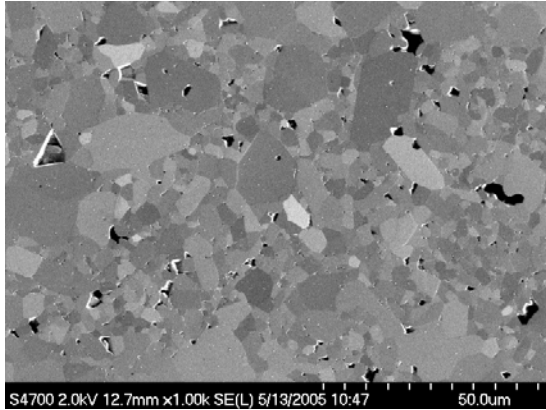


Figure 1. SEM of AD995 (M. Motyka, ARL).

### 3. EXPERIMENTAL METHODS

Three independent sets of experiments were performed to determine: (i) the shock wave response of AD995 under compression (to 18 GPa), and subsequent release, and tension to determine global compressibility, shear and spall (tensile) strengths using piezo-resistive gages and velocity interferometer (VISAR) under a single shock, (ii) the response of AD995 under repeated shock wave compression and subsequent releases to 10.5 GPa, and (iii) the nature of deformation on meso to nm scale from shock recovered AD995.

Shock wave experiments were performed on 10 and 5 cm diameter single stage light gas guns at ARL and RMCS, respectively to determine compression, shear and tensile/spall strengths of AD995. Experiments under two successive shocks were done at ARL to determine the change in compressibility and shear strength of AD995 due to propagation of the first shock wave. Shock recovery experiments were performed at RMCS. Readers are referred to Dandekar and Bartkowski (1994), Dandekar (2001), Cooper et al. (2006), and Bourne et al. (2006) for the design, configuration, and diagnostic details of these experiments<sup>1</sup>.

These experiments were carried out in the stress regimes where AD995 deformed globally in elastic

<sup>1</sup> Page limitation does not permit us to give details of these experiments.

manner and the regime where AD995 deformed inelastically. The boundary between these two regimes is nominally called the Hugoniot Elastic Limit (HEL) [Figure 2]. The HEL of AD995 is 6.7 GPa. Shock recovery experiments on AD995 were performed at 4, 6, and 7.8 GPa, i.e., the stress regime where AD995 deforms globally as an elastic solid and an elastic-plastic solid. Shock recovered specimens of AD995 were examined under optical microscopy (OM), X-ray computed tomography (XCT), Field Emission Scanning Electron Microscopy (SEM) and, Transmission Electron Microscopy (TEM) to determine details of shock wave induced deformation in the material i.e., the nature of deformation of AD995 at different length scales. Resolutions of OM, and XCT vary from microns to mm, while the resolution of SEM and TEM vary between few nm to a few microns. The results of these shock wave experiments permit us to link the observed global deformation of AD995 to deformation at various length scales below and above the HEL

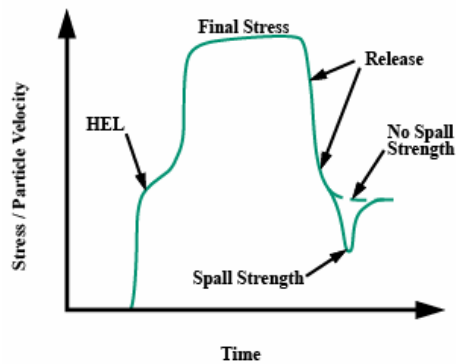


Figure 2. Idealized shock wave profile in elastic-inelastic material. Final stress corresponds to the inelastic stress in the material.

OM and XCT characterizations of shock recovered specimens were done at ARL. SEM and TEM characterizations of the recovered AD995 were done at Johns Hopkins University, Maryland and Tohoku University, Japan.

### 4. SHOCK RESPONSE OF AD995

Shock wave experiments, when appropriately designed, yield values of mechanical properties i.e., compressibility, shear and the tensile/spall strengths as a function of stress. The stress ( $\sigma$ )- volume ratio ( $V/V_0$ ), where  $V_0$  is the initial volume, defines the Hugoniot of a material (Fig. 3). The compression from Equation of State is hydrodynamic or mean stress compression of the material. The magnitude of shear strength may be calculated in two ways: either from the difference between the shock hugoniot stress,  $\sigma (V/V_0)$ , and the

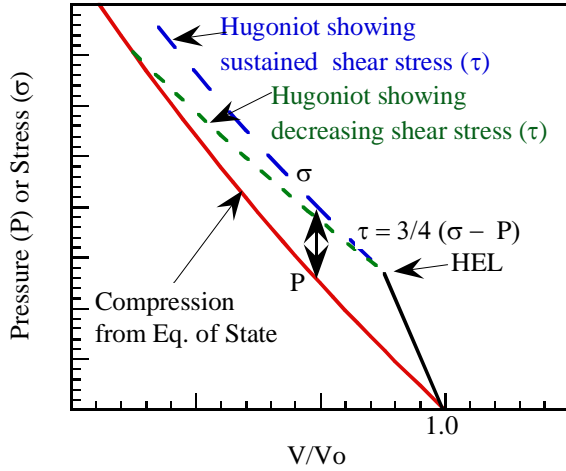


Figure 3. A schematic of shock Hugoniot and hydrodynamic compression of a solid material.

hydrodynamic pressure,  $P(V/V_0)$ , at given compression ( $V/V_0$ ) or from the concurrent measurements of the Hugoniot stress and lateral stress at a given compression. A schematic of the compressive behavior of a material under hydrodynamic compression and plane shock wave compression is shown in Fig. 3. The value of the shear strength [ $\tau(V/V_0)$ ] at a given compression is given by:

$$\tau = 0.75[\sigma(V/V_0) - P(V/V_0)] \quad (1)$$

And from lateral stress ( $\sigma_y$ ) measurements, the value of shear strength is obtained from

$$\tau = 0.5[\sigma(V/V_0) - \sigma_y] \quad (2)$$

Thus the shear strength determined is independent of any assumption about the nature of the inelastic deformation of the material. Fig. 3 shows trends in the magnitudes of shear strength as a function of impact/Hugoniot stress for materials which do not suffer a loss of shear strength ( $\tau > 0$ ) and those which do ( $\tau \rightarrow 0$ ).

Spall strength of material is obtained from the difference in the magnitude of stress between Final stress and Spall strength shown in Fig. 2.

Figures 4 and 5 show a few representative shock wave profiles recorded in compression-spall and lateral stress experiments performed on AD995, respectively. Fig. 4 shows that plastic wave is not fully developed when AD995 is shocked to 11.1 GPa although the HEL, as indicated by the break in the slope of the wave profiles, is clearly seen recorded at 8.4 and 11.1 GPa. The Hugoniot Elastic Limit (HEL) of AD995 is found to be  $6.71 \pm 0.08$  GPa. The tensile/spall strength of AD995 declines with an increase in the magnitude of shock

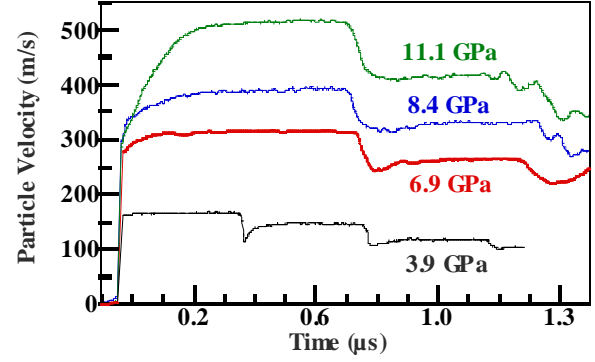


Figure 4. Shock wave profiles in AD995.

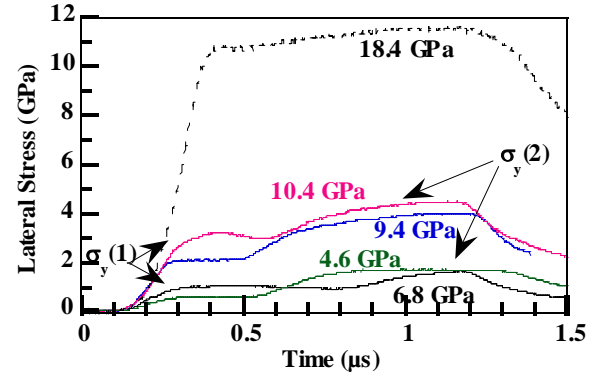


Figure 5. Lateral stress profiles in AD995

induced stress ultimately vanishing between 8.4 and 11.1 GPa.

### Elastic Compression

Dandekar and Bartkowski (1994) reported the Hugoniot Elastic Limit (HEL) of AD995 to be  $6.67 \pm 0.24$  GPa. Grady (Personal communication) reported a value of 6.5 GPa for the HEL of AD995. Dandekar (2001) performed double shock experiments on AD995 to probe the nature of deformation of AD995 at 6.8 and 10.4 GPa. Dandekar found that both the amplitudes and widths of the stress wave profiles in AD995 due to first and second shock with their respective releases are identical when shocked to  $6.78 \pm 0.17$  GPa. Ewart and Dandekar (1994) showed that with the currently used diagnostic in shock wave experiments it is not possible to detect a small volume change, i.e. compressibility of a material under shock wave propagation due to pore closure or generation and growth of small number of cracks and their lengths. The compression duration of the first and second shock wave was  $0.37 \mu s$ . The second shock propagated in AD995 after the stress generated by the first shock was totally released. This result implied that global and dominant deformation of AD995 at 6.78 GPa was elastic and reversible i.e., the stress and strain states were attained through elastic deformation. The associated values of density and particle velocity at the

HEL are  $3.940 \pm 0.004 \text{ Mg/m}^3$  and  $0.162 \pm 0.005 \text{ km/s}$ , respectively. Reinhart and Chabbildas (2003) report values of HEL varying from 6.7 to 7.89 GPa.

### Inelastic Compression

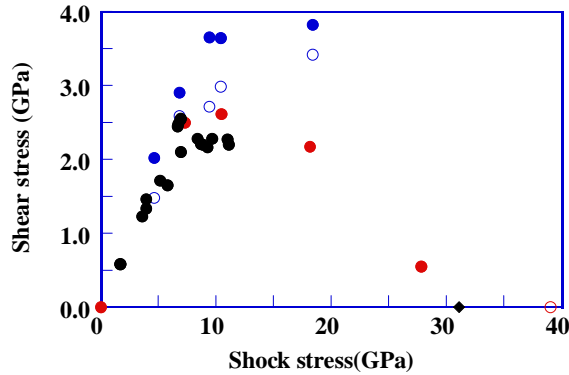


Figure 6. Shear stress sustained in AD995 with shock induced stress. solid and hollow symbols; RED: Grady (Personal communication) and, Reinhart and Chhabildas (2003), Blue: Cooper et al. (2006), Black Dandekar and Bartkowski (1994).

Fig. 6 shows the variation in the value of shear stress sustained in AD995 as function of shock induced stress. Results obtained by Dandekar and Bartkowski (1994) and by Grady (Personal communication) from the offset between the shock Hugoniot and hydrodynamic compression suggest that deformation of AD995 above its HEL is elastic-plastic to around 12 GPa. Above 12 GPa, AD995 begins to possess a decreasing magnitude of shear strength with an increase in shock stress. However, the results of lateral stress measurements indicate AD995 continues to maintain increasing shear strength to 18.5 GPa. Shock data of Grady show that AD995 suffers a total loss of shear strength around 31 GPa. Reinhart and Chabbildas (2003) found that AD995 has no shear strength at and above 39 GPa. The discrepancy in the shear strength values of AD995 obtained from the offset between the shock Hugoniot and hydrodynamic compression and lateral stress measurement remains to be resolved. However, the discrepancy does not impact the results of the current work dealing with the determination of nature of deformation from the existing shock wave data and features observed in the of shock recovered AD995 by means of optical microphotography (OM), X-ray computed tomography (XCT) and, transmission electron microscopy (TEM).

### Spall Strength

Spall strength of AD995 is impulse dependent (Table 1). For instance, at the HEL, 6.7 GPa, of AD995, the values of spall strengths are 0.31, 0.37, and 0.46 GPa for compressive pulse durations/pulse width of

approximately 0.70, 0.35, and 0.16  $\mu\text{s}$  respectively. The dependence of spall strength on the pulse width is evident even when AD995 is shocked to as low as 1.7 GPa or as high as 9.27 GPa. In general, spall strength of AD995 decreases with an increase in both the magnitudes of shock compressive stress and their durations. For example, spall strength declines from a value of 0.46 GPa to 0.295 GPa at shock induced stress of 1.7 GPa and 8.4 GPa for a pulse width of around 0.7  $\mu\text{s}$ . Spall strength vanishes at 8.8 GPa for a pulse width of 0.7  $\mu\text{s}$ . The decrease in the value of spall strength at and below the HEL irrespective of the pulse widths between 0.16 and 0.7  $\mu\text{s}$  suggests an increase in the population of micro-cracks in AD995 under shock compression and release even when shocked to as low as 1.7 GPa prior to generation of tensile stress as a result of release wave interaction in AD995. Diminution of the spall strength of AD995 is attributed to dominant brittle character of AD995.

**TABLE 1.** AD995 Spall Strength .

Shot #	Impact Velocity (km/s)	Pulse Width ( $\mu\text{s}$ )	Impact Stress (GPa)	Spall Strength (GPa)
213	0.0829	0.743	1.70	0.458
307	0.0780	0.369	1.67	0.612
240	0.175	0.720	3.79	0.387
303	0.182	0.354	3.91	0.568
234	0.251	0.687	5.36	0.421
329	0.295	0.783	5.69	0.357
224	0.349	0.699	6.94	0.306
313	0.323	0.349	6.93	0.367
314	0.320	0.165	6.71	0.456
331	0.313	0.165	6.49	0.476
229	0.433	0.694	8.35	0.295
304	0.465	0.671	8.82	-
309	0.418	0.342	8.63	0.331
236	0.512	0.709	9.53	-
310	0.450	0.338	9.27	0.247
301	0.597	0.702	10.84	-
239	0.604	0.697	11.04	-

## 5. SHOCK RECOVERED AD995

Design of shock recovery experiments ensured that AD995 specimen was subjected to a single shock wave compressive stress of a predetermined magnitude followed by release of the compressive stress before the effects of lateral stress release distorted the compressive and release histories especially in the central region of the AD995 specimen. Further, the design ensured that no tension developed in AD995 due to wave interactions. Thus the observed features in the recovered AD995 could be unambiguously associated with the shock induced planer shock compression and release.

### Optically Observed Features: scale 1mm – 1 cm

Photographs of the three sets of samples in their brass holders are shown in Figure 7. Figure 8 shows the macro-crack pattern of damage observed in the recovered, centrally sectioned and dye penetrated alumina discs. The sectioned surface of the disc that was subjected to the 4 GPa shock was coated with a transparent resin, which alters its fractographs. Broadly, the network of macrocracks consists of horizontal and vertical fissures, resulting in numerous fractured material blocks populating the specimen volume. The specimens subjected to the higher shock stresses show marked evidence of a higher macrocrack density in the central region. Fracture planes that traverse the entire specimen width are also seen in Figure 8, and notably, a fracture cavity is present on the impact surface of the specimen subjected to a shock compression of 7.8 GPa. However, it is difficult to assess the volume occupied by the cracks at these stresses. The population and size of macrocracks does help to understand the observed decrement of spall strength of AD995 with increase in the magnitude of shock induced stress and its duration.



Figure 7. Recovered samples in brass holders.

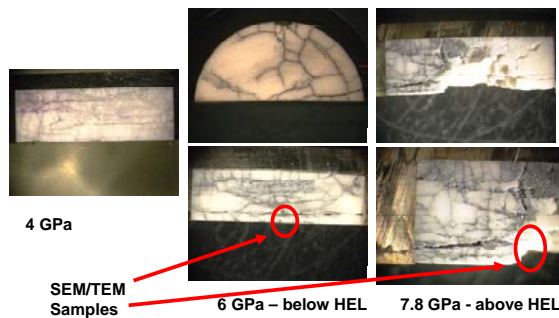


Figure 8. Optical Microscopy of Stained fracture patterns in cross section and top view (6 GPa)

#### X-ray Computed Tomography: scale 0.1 mm – 1 cm:

X-ray computed tomography (XCT) may be applied to any material through which a beam of penetrating radiation may be passed and detected, including metals, plastics, ceramics, metallic/non-metallic composite material, and assemblies. The principal advantage of XCT is that it provides densitometric images of thin cross sections through an object. Because of the absence of structural superimposition, images are easier to interpret than conventional radiological images. Further,

because XCT images are digital, the images may be enhanced, analyzed, compressed, archived, input as data to performance calculations, compared with digital data from non-destructive evaluation modalities, or transmitted to other locations for remote viewing, or a combination thereof.

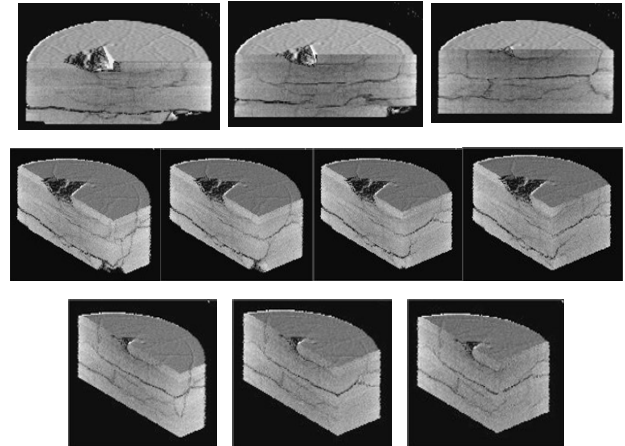


Figure 9. Three-Dimensional (3-D) virtual solid images of 6 GPa sample with sections cut away

A sectioned half-disk from each recovered sample was inspected using a customized XCT system (scanner) at the U.S. Army Research Laboratory (ARL). It has a 420 keV X-ray tube with two focal spot sizes and a 225 keV microfocus X-ray tube with a variable focal spot size down to 5  $\mu\text{m}$ . A dedicated embedded industrial computer system controls object scanning (*i.e.* data collection) and image reconstruction, viewing, and processing.

The sample was scanned parallel to its faces, making the cross-sectional image plane perpendicular to the through thickness direction. Each sample was scanned from its impact side (in contact with the cover plate) to its rear face. Each slice was reconstructed to a 1024 by 1024 image matrix collecting 3600 views (*i.e.* projections) during the full rotation and with about 60 slices required to completely scan each sample. The tube energy and current used were 160 keV and 0.035 mA, respectively, and the focal spot was 20  $\mu\text{m}$ .

Bourne et al. (2006) describe, and present in detail, results of XCT scans done on the recovered specimen of shocked AD995 to 6 GPa. The excellent dimensional accuracy and the digital nature of XCT images allow the accurate volume reconstruction of multiple adjacent slices. Figure 9 shows a series of three-dimensional solid images of the 6 GPa sample with various sections virtually removed. The top three images are looking down at the sectioned side of the sample with it tilted 25° to the impact side: top left is just inside the actual surface, the next two are 1 and 2 mm from the actual

surface; the next four images have been rotated 50° about the z axis with the distances on the right from the corner being 2.3, 3.3, 4.4, 5.4 mm respectively; the last three images are similar to the previous four, but sectioned at closer to the edge of the sample, at 2.3, 4.4, and 6.4 mm from the actual sample corner.

A three-dimensional, reconstructed solid of the virtual damage distribution within the sample, in which the undamaged material is made partially transparent to view the damaged areas indicated in white, is shown in Fig.10. The impact side of the original sample in this view is below the sectioned face as indicated by the large white area on the bottom.

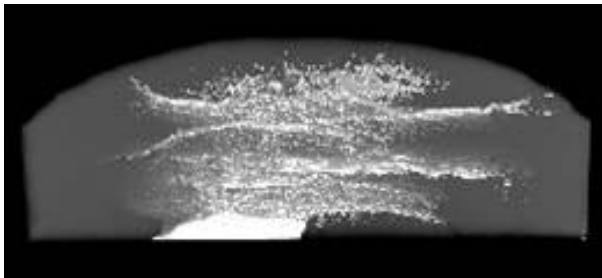


Figure 10. 3-D virtual solid of damage distribution

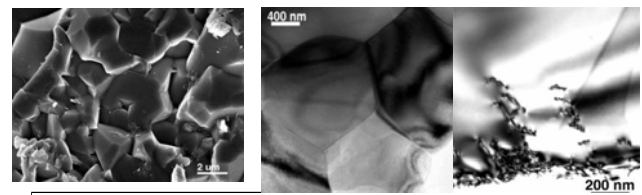
**SEM and TEM Features: scale = 10 μm – 1 nm:**

The deformation and failure mechanisms operating in shock-loaded AD995 alumina were systematically investigated by employing scanning electron microscopy (SEM) and transmission electron microscopy (TEM) [Chen et. al. 2006]. Two samples subjected to shock-induced stresses of 6.0 GPa and 7.8 GPa (below and above its HEL of 6.7 GPa) were separately sectioned and imaged (Fig. 8).

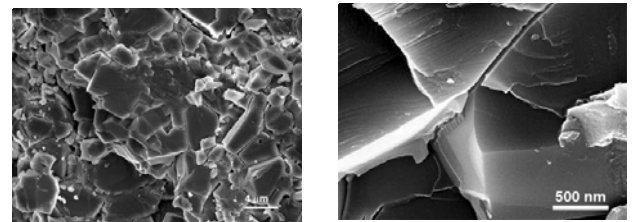
SEM observations suggest a transition in fracture behavior from intergranular-dominated fracture (at a stress of 6 GPa below the HEL) to cleavage-dominated (at 7.8 GPa above the HEL). Fig. 11 (a). shows a SEM micrograph taken from the 6 GPa sample. The fracture surface corresponds to individual grains with smooth facets, suggesting failure along grain boundaries (GBs). SEM micrographs of the fragment surfaces (see Fig. 12 (a) and (b) show failure of the 7.8 GPa specimen is dominated by transgranular fracture. Typical cleavage features including river patterns and cleavage steps along specific crystal directions, can be identified in Fig. 12(b).

A majority of grains in AD995, subjected to 6 GPa, did not exhibit plastic deformation on the faceted surfaces. Occasionally, dislocations can be found in the vicinity of grain boundaries as seen the bright-field TEM micrograph in Fig.11 (c). The dislocations and dislocation arrays most likely emitted from a grain boundary are characterized as normal dislocations.

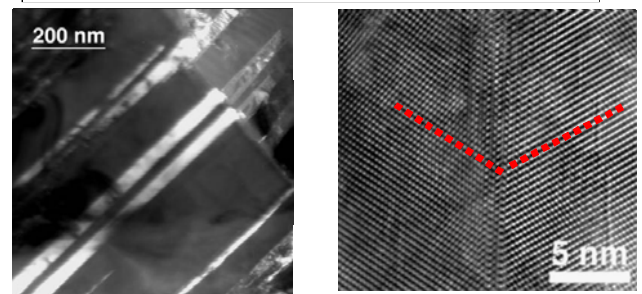
Both SEM and TEM observations indicate that the 6.0 GPa specimen experienced mainly elastic deformation during shock loading. The limited plastic deformation in the vicinity of GBs found by systematic TEM characterization may be produced by localized stress concentrations arising from the propagation of GB cracks, defects at grain boundaries, or grain-to-grain elasticity mismatch, which promote the nucleation of the observed dislocation. Because concentrated stresses always degrade quickly from GBs, the generated dislocations may not be able to move too far from their sources at GBs, only resulting in local plastic deformation. Apparently, this localized plasticity cannot significantly affect the overall elastic response of the material to the applied shock loading.



(a) (b) (c)  
Figure 11. SEM and TEMs of 6 GPa sample: a.) SEM in uncracked area; b.) TEM in uncracked area and c.) TEM in cracked area



(a) (b)  
Figure 12. SEMs of 7.8 GPa sample



(a) (b)  
Figure 13. TEMs of 7.8 GPa sample

Dramatic changes in the deformation mode behavior were found in the AD995 alumina specimen experiencing an impact pressure of 7.8 GPa. TEM characterization suggests that numerous deformation twins appear in a large number of grains as illustrated in Fig.13 (a) and (b). The twin bands in each grain parallel each other along a common crystallographic orientation, suggesting only one slip system was activated in each

grain during shock loading. In the dark-field TEM micrograph, twin dislocations can be identified within the twin bands. They were determined to be  $1/3[1010]$  partial dislocations. High-resolution electron microscope (HREM) characterization shows that the width of the twin bands ranges from several to tens of nanometers (Fig.13 (a)) and the twin interfaces contain a large number of twinning dislocations [Figure 13(b)]. HREM image simulations suggest that the twinning is along the basal plane (0001) of the hexagonal unit cell. Thus, these deformation twins are determined to be the basal twins. The critical shear stress ( $\tau_c$ ) for the formation of deformation twins in perfect alumina crystals can be roughly estimated according to a simple equation (Hirth and Lothe, 1982).

$$\tau_c = \frac{\gamma}{b_P} \quad (3)$$

where  $b_P$  is the magnitude of the Burgers vector of the twin dislocations and  $\gamma$  is the stacking fault energy. The estimated critical shear stress ranges from 5-8 GPa, which is in the same magnitude of the HEL of alumina (4~16 GPa) reported so far and very close to the one half of the HEL values of the polycrystalline alumina with high purity and density. This suggests that the twinning driven by the shear component of the uniaxial shock compression stress appears to be responsible for the elastic-to-inelastic transition at the HEL.

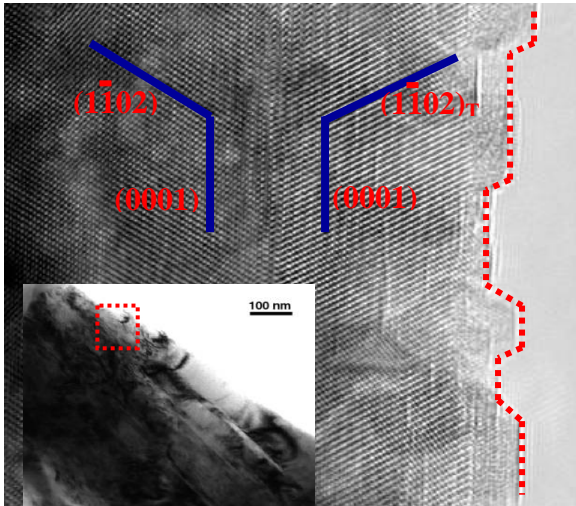


Figure 14. . Lattice image of a thin fragment. The faceted edge is mainly parallel to (0001) basal plane. The cleavage steps marked in the figure are either parallel to the matrix (1-102) plane or to the (1-102) plane of the twin band.

It is interesting to note (Fig.14) that the edges of the 7.8 GPa fragments are frequently faceted on (0001)

twinning planes, indicating an intrinsic correlation between deformation twins and the cleavage failure. The HREM image taken from a recovered specimen exhibits a faceted edge that appears along an interface of the twin band shown in the lattice image. The edge is mainly along (0001) basal planes with steps parallel to (1-102) plane of either the matrix or the twin band, as indicated by the dashed line. The apparent cleavage along (0001) twin planes and the appearance of (1-102) planes of both twin and matrix as the cleavage steps, suggest that the fracture is along the interface of the twin bands during shock loading or unloading. It appears that the generation of deformation twins in the shock-loaded alumina provides a shortcut, or energetically more favorable path, for cleavage cracking and thereby a change in the fracture mode from intergranular behavior to transgranular cleavage.

It has been well known that shock, i.e. high rates of load application and release, favors twin formation in a number of materials, probably due to rate sensitive inertial effects. The process of twinning can form in time periods as short as a few microseconds, while for slip accomplished by normal dislocation gliding there is a delay time of several milliseconds before a slip band is produced. The slip process by dislocation gliding seems to be resistant to shock loading, that is, the movement of dislocations for appreciable distance requires that the stress is applied for a considerable time period. In crystals with high plastic slip resistance, such as ceramics, under uniform levels of stress, twins can propagate with near sonic velocity. Recent molecular dynamics simulations also suggest that dislocation motion at high strain rates become jagged, resulting in spontaneous self-pinning. Then, at still higher strain rates, the dislocation stops abruptly and emits a twin plate that immediately takes over as the dominant mode of plastic deformation. Twinning requires a high concentration of strain energy and this should be readily available during shock loading. The elastic strain energy stored during ramp up to the HEL will drive the twinning movements even after the passage of the shock wave when the time periods of shock loading is shorter than the twinning process. Cracking along twinning interfaces has been observed in a number of brittle materials and various explanations have been proposed. For the case of shock-loaded AD995 alumina, it is most likely that the cleavage along the twin boundaries is caused by the deviatoric stresses applied to the twin bands during unloading and the relative weak chemical bonding at the non-relaxed twinning interfaces.

## 6. DISCUSSION

The observations in this study provide compelling experimental evidence for the micromechanism

responsible for shock induced global plastic deformation in AD995 alumina. The HEL appears to be associated with the onset of deformation twinning, which drives the primary fracture mode from an intergranular one (below the HEL) to transgranular cleavage above HEL. The correlation of HEL with micro-plasticity and fracture can be represented in the schematic shown in Figure 15.

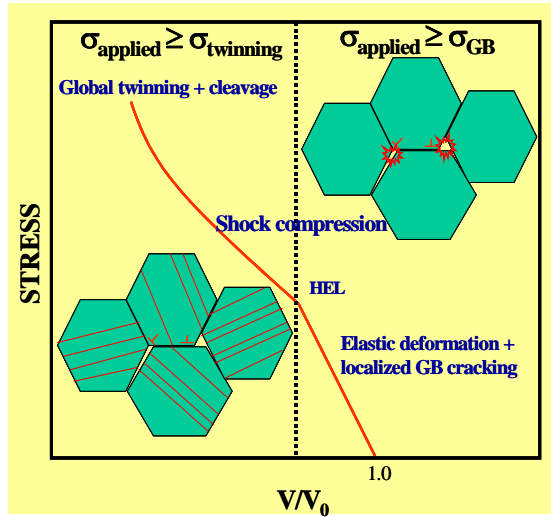


Figure 15. Schematics of the correlation of HEL with micro-plasticity and cracking, in which  $\sigma$  is shock stress,  $\sigma_{gb}$  is the cohesion of grain boundaries, and  $\sigma_{twin}$  is the critical stress for twinning.

When the impact velocity is such that the induced stress is below HEL, deformation twins are not activated. However, it may be high enough to cause intergranular fracture and the formation of dislocations in the vicinity of GBs, seemingly produced by stress concentrations caused by GB crack propagation, existing GB flaws or grain-to-grain elasticity mismatch. Since they are localized and discontinuous, the cracking and dislocation gliding are not expected to significantly affect the overall primarily elastic response of the material as shown to be the case under compression and release. However, under shock generated tension, the deleterious effect of cracking is significant even at as low a stress as 1.7 GPa as evident from the pulse width dependence of the spall strength of AD995. At stresses greater than the HEL, the applied stresses are higher than the critical stresses for twinning. Thus, deformation twins can be activated in a large number of grains prior to the GB cracking. This global plastic deformation causes the inelastic response and the twinning planes provide an easy means for cleavage fracture, giving rise to a change in the fracture morphology. Finally, the OM, XCT, SEM and TEM characterizations of the shock recovered AD995 provides an opportunity for modeling of the material at varying length scales to reproduce the shock response of AD995

obtained from shock wave experiments at the continuum scale.

## REFERENCES

- Barker, L. M. and Hollenbach, R. E., 1970: Shock Wave Studies of PMMA, Fused Silica, and Sapphire, *J. Appl. Phys.* Vol. 44, 4208-4226.
- Bourne, N. K., Green, W. H., and Dandekar, D. P., 2006: On the one-dimensional recovery and microstructural evaluation of shocked alumina, *Proc. of the Royal Soc. A.* published on line 2006 and references therein.
- Chen, M.W., McCauley, J. W., Dandekar, D.P., and Bourne, N. K., 2006: Dynamic plasticity and failure of high-purity alumina under shock loading, *Nature Materials.* published on line July 2, 2006 and references therein.
- Cooper, G. A., Millett, J. C. F., Bourne, N. K., and Dandekar, D. P., 2006: Delayed Failure in a Shock Loaded Alumina, *Shock Compression of Condensed Matter -2005*, Ed. M. D. Furnish, M. Elert, T. P. Russell, and C. T. White, American Institute of Physics, New York, 847-850 and references therein.
- Dandekar, D. P. , 2001: Deformation of AD995 Alumina Under Repeated Plane Shock Wave Loading, *Impact Engineering and Applications*, Ed. A. Chiba, S. Tanimura and K. Hokamoto, Elsevier, New York, 785-790 and references therein.
- Dandekar, D. P. and Bartkowski, P., 1994: Shock Response of AD995 Alumina, *High-Pressure Science and Technology-1993*, Ed. S. C. Schmidt, J. W. Shaner, G. A. Samara, and M. Ross, American Institute of Physics, New York, 733-736 and references therein
- Ewart, L. and Dandekar, D. P., 1994: Relationship between the Shock Response and Micro-structural Features of Titanium Diboride *High-Pressure Science and Technology-1993*, Ed. S. C. Schmidt, J. W. Shaner, G. A. Samara, and M. Ross, American Institute of Physics, New York, 733-1201-1204.
- Hirth, J. P. and Lothe, J., 1982: *Dislocation Theory* John Wiley & Son, Inc., New York, 2<sup>nd</sup> edition, 811-833.
- Reinhart, W. D. and Chhabildas, L. C., 2003: Strength Properties of Coors AD995 Alumina in the Shocked State, *Int. J. Impact Eng.* 29, 601-609 and references therein.



# 25<sup>th</sup> Army Science Conference

*“Transformational Army Science and Technology*

*- Charting the Future of S&T for the Soldier”*

**“Global Mechanical Response and its Relation to Deformation and Failure Modes at Various Length Scales under Shock Impact in Alumina AD995 Armor Ceramic”**

D. P. Dandekar, J. W. McCauley and W. H. Green, U.S. Army  
Research Laboratory

M. Chen, Johns Hopkins University/Tohoku University, Japan

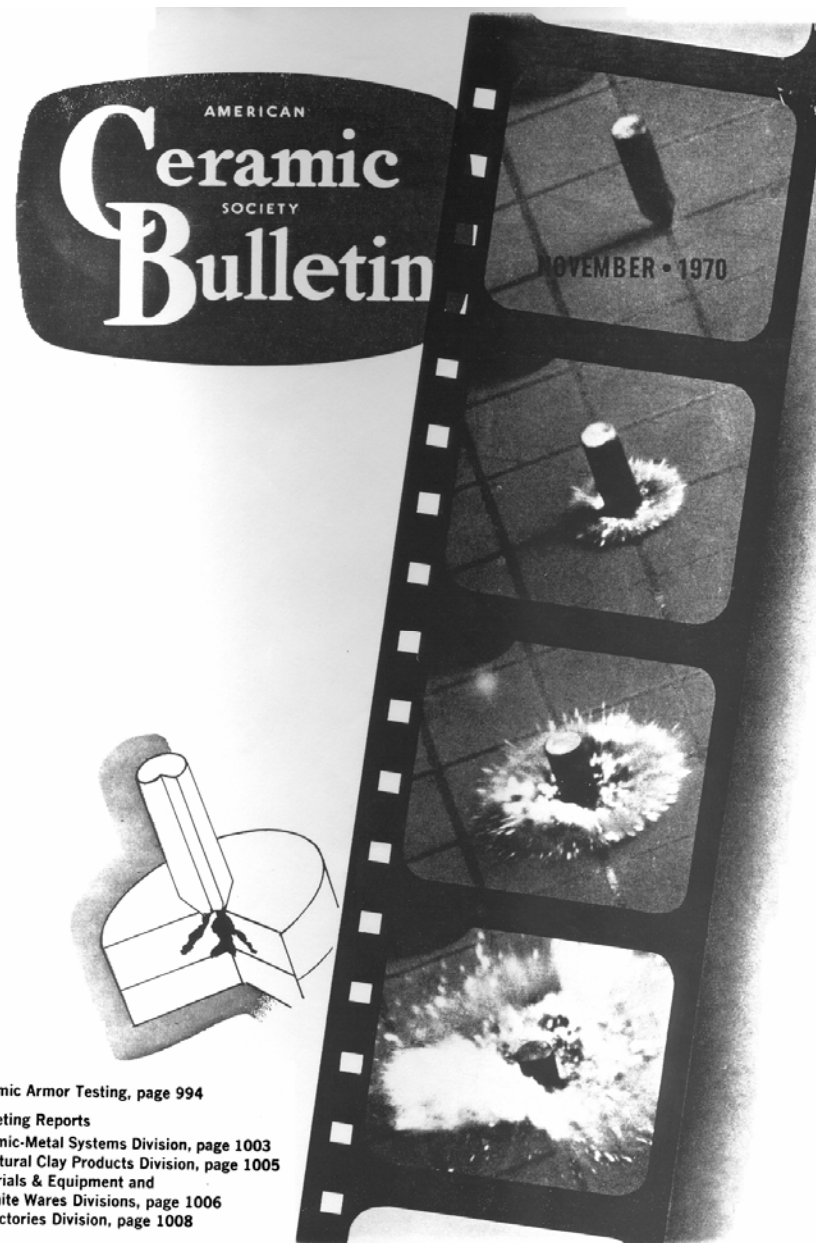
N. K. Bourne, University of Manchester, UK

30 November 2006

Orlando, Florida



**McCauley et al. 2004**



Ceramic Armor Testing, page 994  
Fall Meeting Reports  
Ceramic-Metal Systems Division, page 1003  
Structural Clay Products Division, page 1005  
Materials & Equipment and  
White Wares Divisions, page 1006  
Refractories Division, page 1008

**Frechette and Cline, 1970**

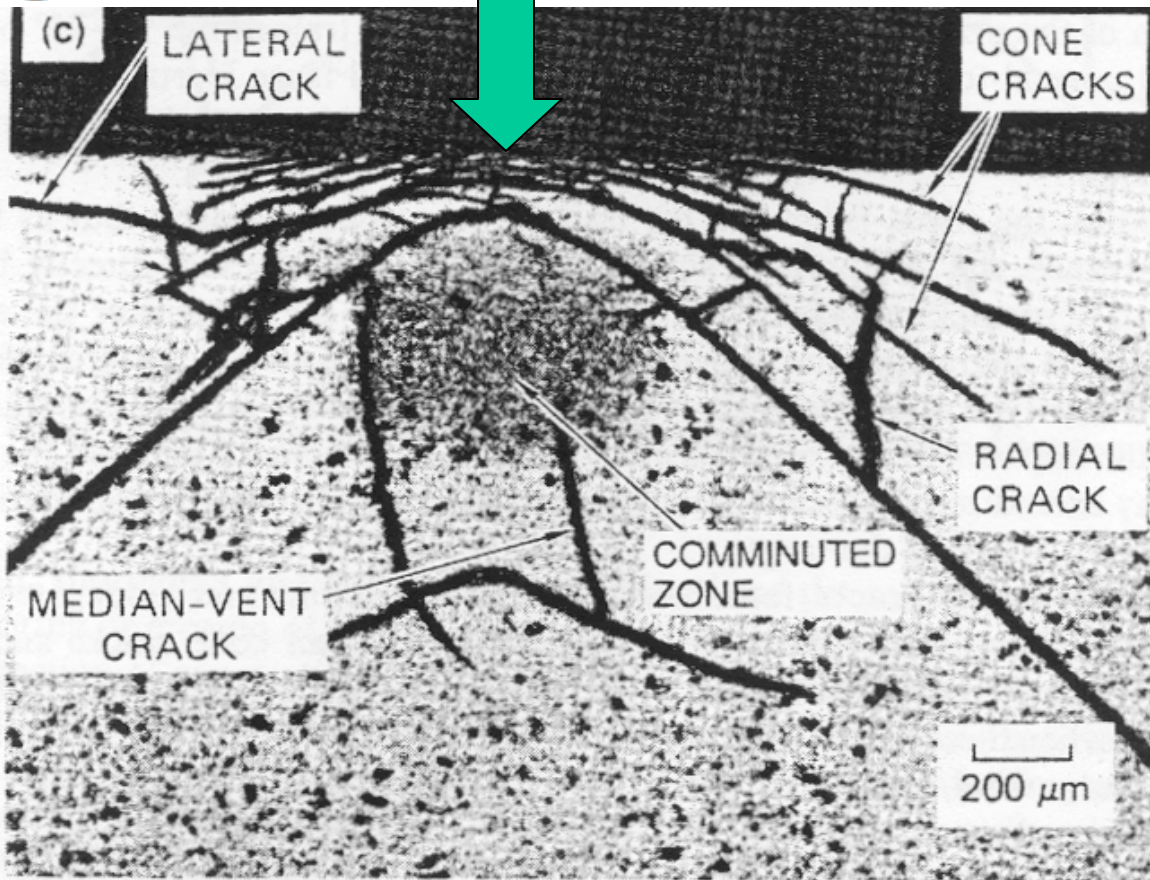


# OUTLINE

- Ballistic event background
- Plate impact background and soft recovery experimental details
- Global mechanical response at all length scales
  - Macro damage: optically observed features: scale 1mm – 1 cm.
  - Macro to micro damage: X-ray computed tomography: scale 0.1 mm – 1 cm.
  - Micro to nano deformation and damage: SEM and TEM Features:  
scale = 10  $\mu\text{m}$  – 1 nm.
- Summary and conclusions



# Simplified Armor Ceramic Ballistic Impact Event



## Energy Dissipation

- Bullet failure
- Elastic deformation
- Inelastic deformation
- Micro/macro cracking
- *Damage evolution and failure at several length scales*

FIG. 8. Sectional views of subsurface cracking pattern in HP  $\text{Si}_3\text{N}_4$  impacted by 2.4 mm diameter steel spheres at velocities of  $56.4 \text{ m s}^{-1}$  (a) and  $231 \text{ m s}^{-1}$  (b) and by a 2.4 mm diameter tungsten carbide sphere at  $231 \text{ m s}^{-1}$  (c).

Shockey, et al., 1990

Typical Impact Stresses: 10-30GPa



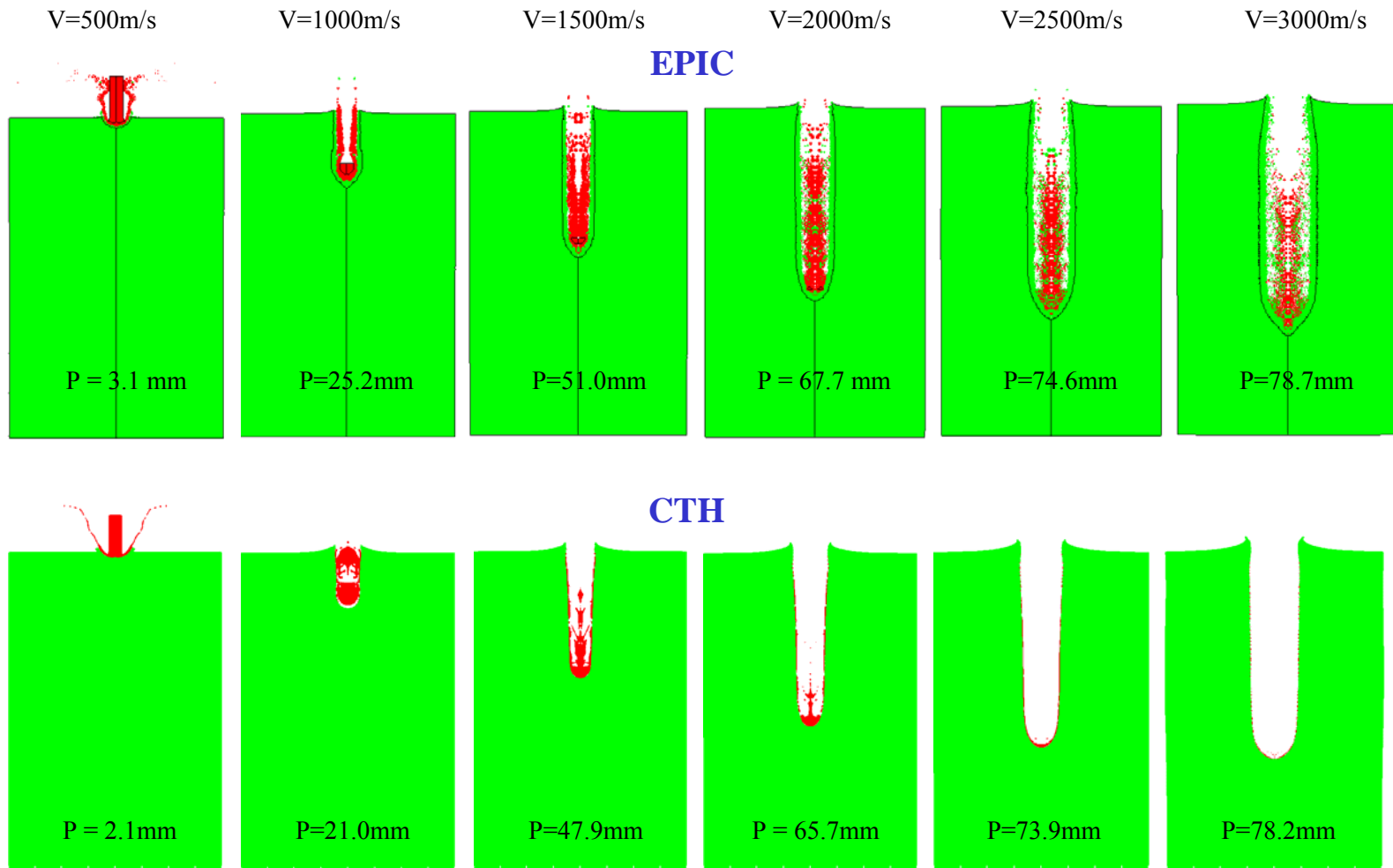
## Simplified Differences between Quasi-static and Ballistic Mechanical Stress Environments on Armor Ceramics



	Quasi-static Bend Bar Stress Environment	Ballistic Stress Environment
Stressed Volume	Typically Small ~12 mm <sup>3</sup>	Huge 15-20,000 mm <sup>3</sup>
Rate and defects	Largest Defect	Many Defects Tail of Distribution
Rate and micro-mechanisms	<ul style="list-style-type: none"> <li>• Partial dislocations</li> <li>• Slip</li> <li>• Toughness</li> <li>• Others</li> </ul>	<ul style="list-style-type: none"> <li>• Deformational Twinning</li> <li>• Amorphization</li> <li>• <b>“Effective Plasticity”</b></li> <li>• Others</li> </ul>
Stress Characteristics	<ul style="list-style-type: none"> <li>• Gradual rise to failure</li> </ul>	<ul style="list-style-type: none"> <li>• <b>Mixed stress states: compression, tension (spall), shear</b></li> <li>• Shear increasing</li> <li>• Hertzian</li> <li>• Shock wave “conditions” material</li> <li>• Over stress condition</li> </ul>



# Semi-infinite penetration using Johnson-Cook material model



PENETRATION PROFILES

Templeton et al, PacRim 2001



## Ultimate Challenge

*“Design Materials for Optimized Armor Performance that Can Adjust to Changing Threats and System Designs”*

**Material Scientists and Engineers Want to Know What They can do to Materials to Make Them Work Better**

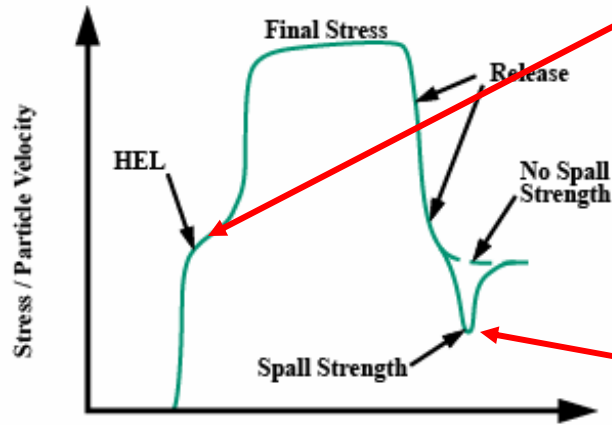


# Issues

- Accelerating optimization of armor ceramics depends on development of validated predictive performance computer models.
- Depends on determination and quantification of the various ballistic energy absorption mechanisms:
  - Deformation modes, damage nucleation and accumulation processes, and the resulting failure at all length scales
- Actual ballistic tests extremely complex and difficult to extract quantitative deformation and failure mechanisms on the armor materials
- Utilize instrumented dynamic tests that can mimic some important aspects of the ballistic event
- **Focus in this work is on soft recovery plate impact experiments on AD 995 Alumina from CoorsTek – a common armor ceramic**

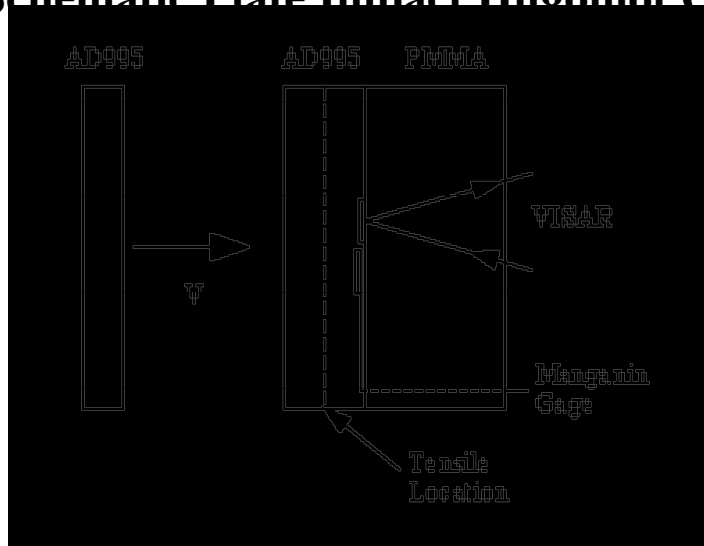


# Plate Impact and Hugoniot Elastic Limit (HEL)

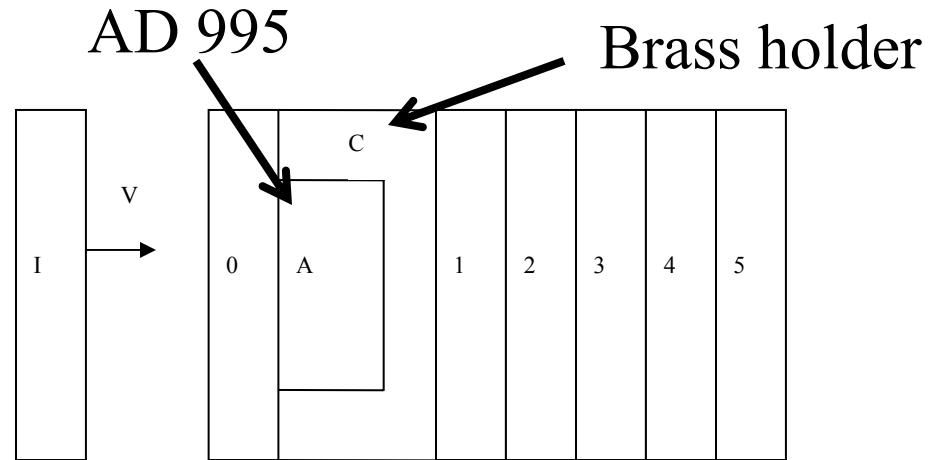


- HEL: transition from primarily elastic deformation to inelastic deformation/plastic (before failure)
- Understanding shear strength and plastic deformation mechanisms in ceramics could lead to improved armor materials
- Spall strength  $\approx$  tensile strength

Schematic Plate Impact Hugoniot Curve



(a) Normal plate impact



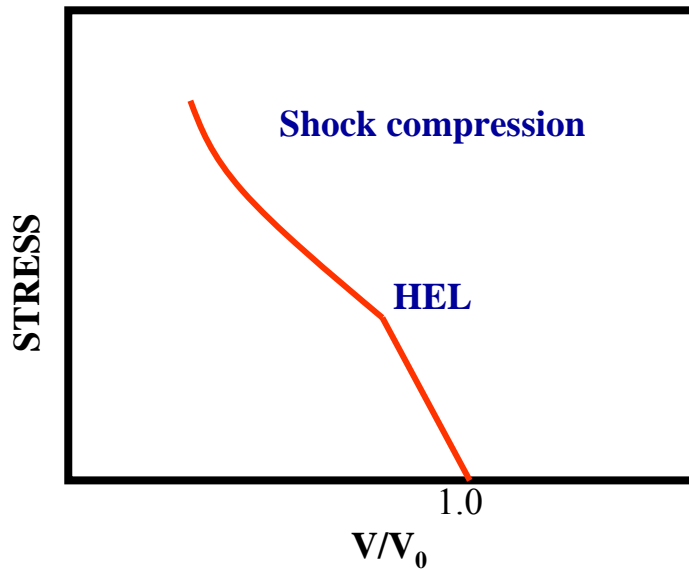
(b) Configuration of a Bourne soft recovery experiment.

Schematics of plate impact configurations.



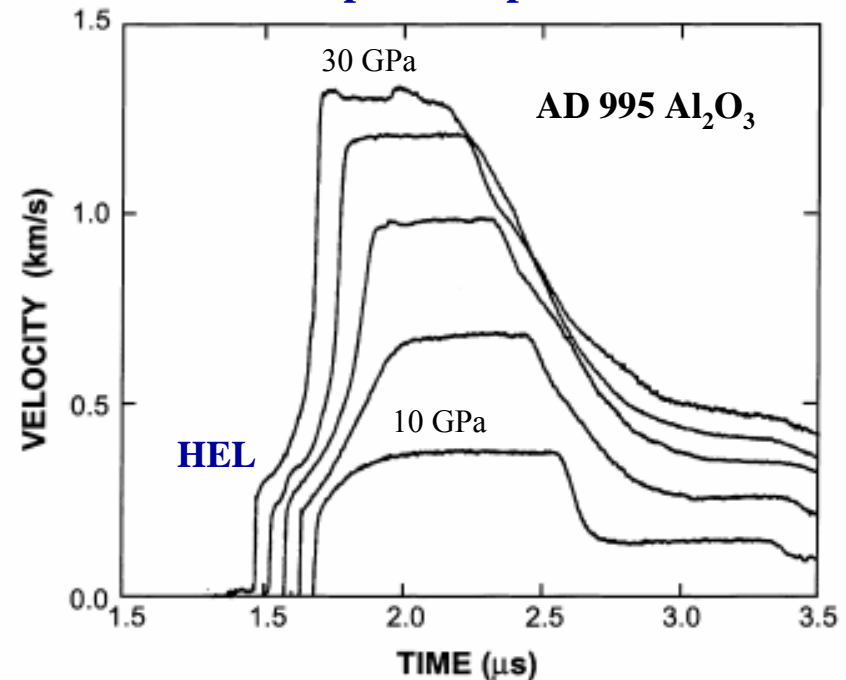
# Hugoniot Elastic Limit (HEL)

Stress-volume trajectory



(Graham, *Solids under high-pressure shock compression*, 1993)

Shock compression profiles

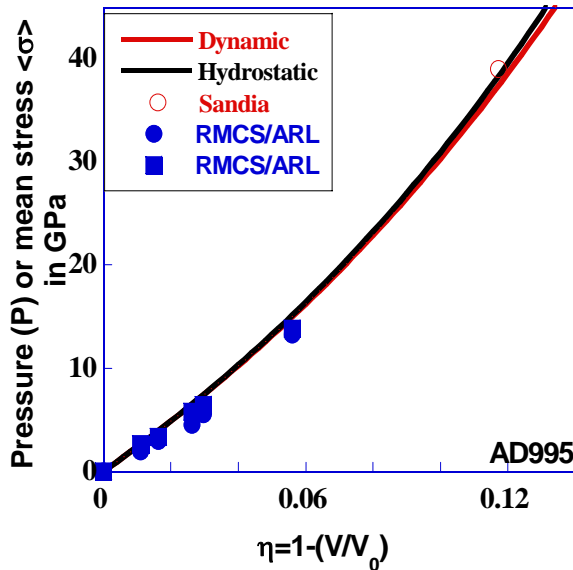


(Grady, *Mechanics of Materials* 29, 181(1998))

HEL = 6.7 GPa for AD 995

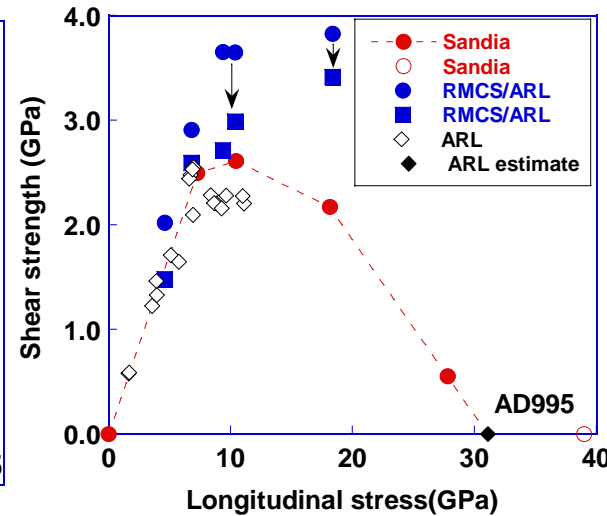


# Global Deformation of AD 995



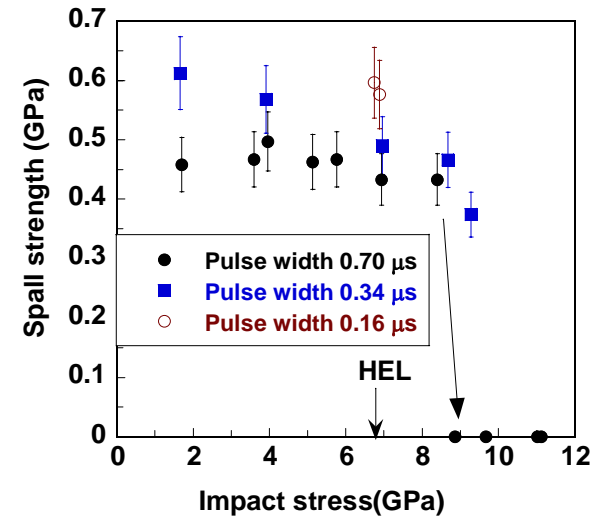
## Compression Strength

Static/dynamic very nearly identical



## Shear Strength

- Increases up to 12 GPa
- Decreases beyond 12 GPa
- Vanishes around 40 GPa.

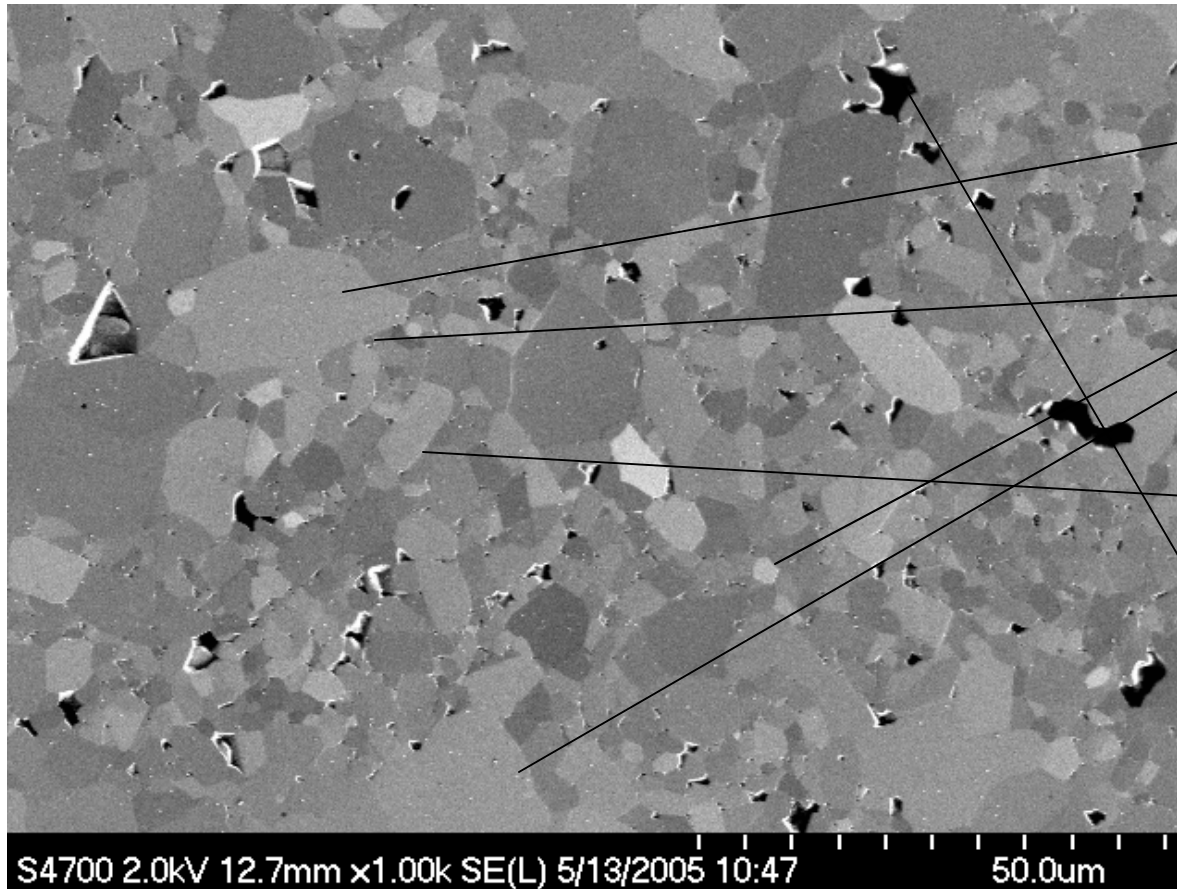


## Spall Strength

- Dependent on shock duration
- Decreases with an increase in shock induced stress
- Defects are generated even at <math>< 6.7</math> GPa.
- No spall strength > 8.5 GPa; no observable cohesion



# AD 995 Alumina



C =  $\text{Al}_2\text{O}_3$

M = grain size distribution

Grain Boundary

PD = processing defect = porosity

FESEM of Polished AD 995 (Alumina)  
Late 1990's vintage material – not CAP 3  
(M. Motyka)



**Macro damage - optically observed  
features: scale 1mm – 1 cm**



## Soft Recovered Plate Impact AD995 Alumina



**4 GPa**

**Below HEL**



**6 GPa**

**Below HEL**



**7.8 GPa**

**Above HEL**



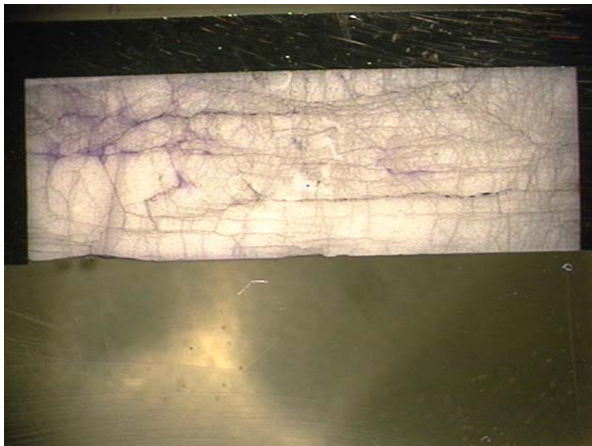


# Macrostructure Characterization of Soft Recovered Plate-Impacted AD995 Alumina



## Macro Crack

## Patterns - Stained

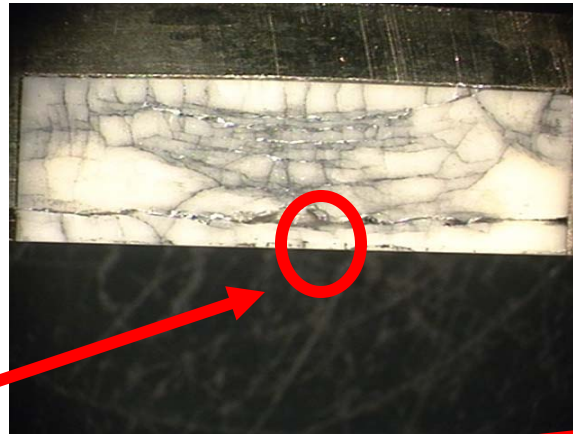


4 GPa

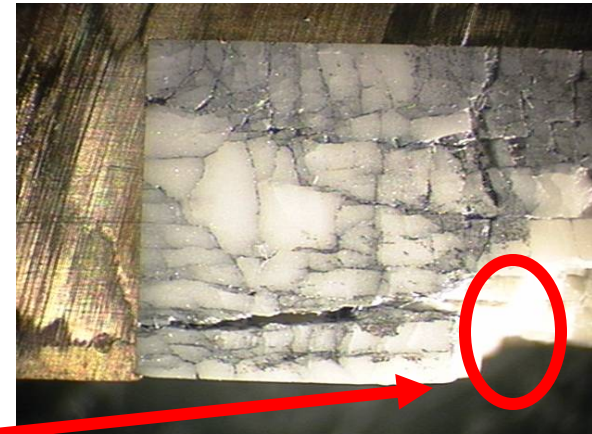
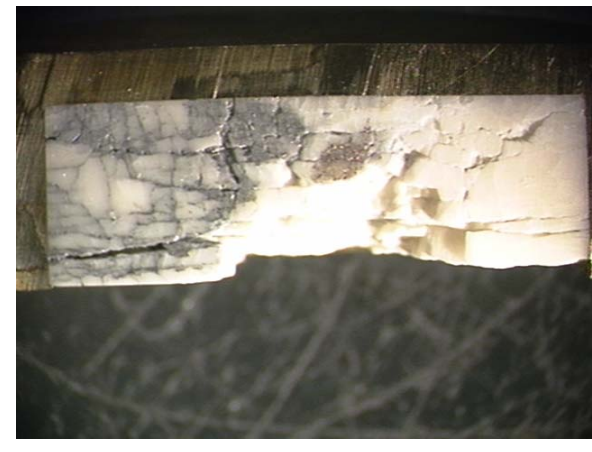


~ 1 inch

SEM/TEM  
Samples



6 GPa – below HEL



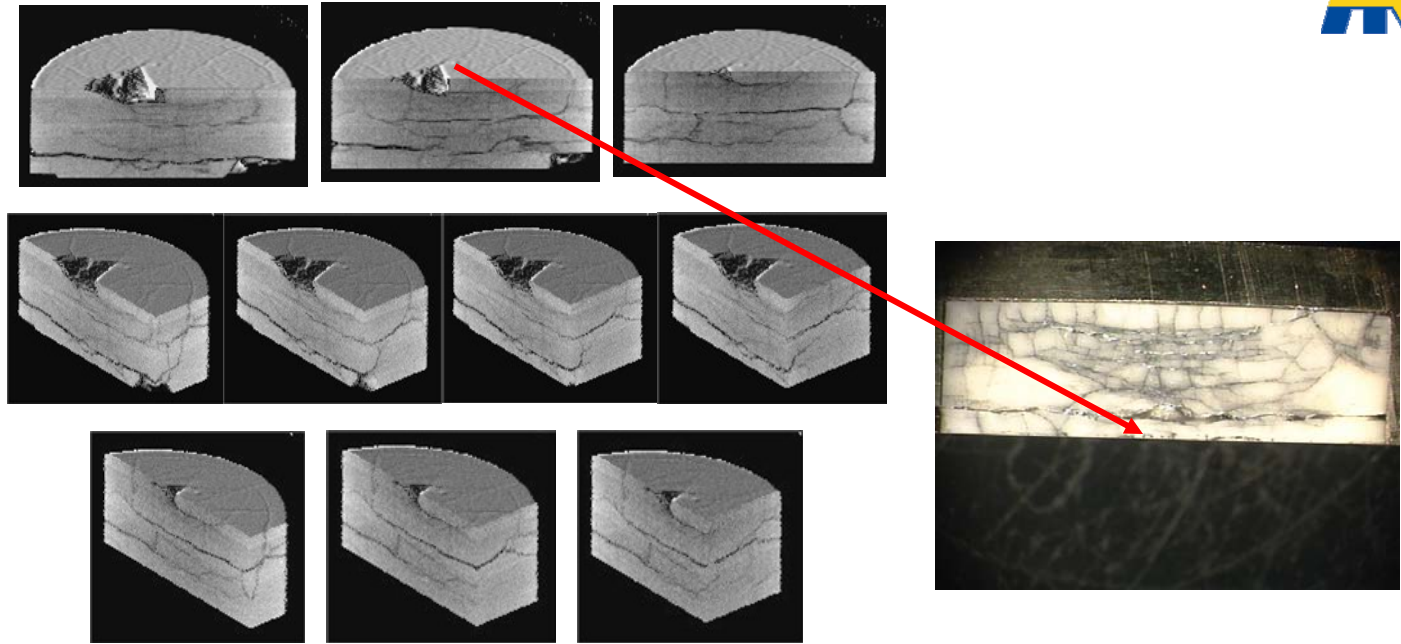
7.8 GPa - above HEL



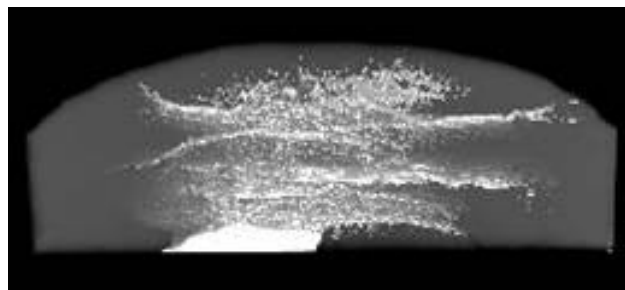
# **Macro to micro damage -X-ray computed tomography: scale 0.1 mm – 1 cm**



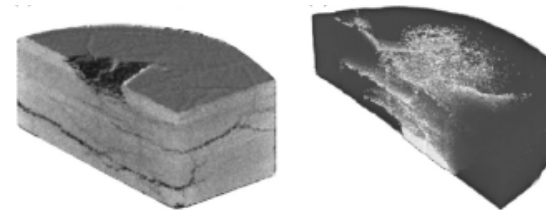
# X-ray Computed Tomography of 6 GPa Sample



Three-Dimensional (3-D) virtual solid images of 6 GPa  
sample with sections cut away



3-D virtual solid of damage distribution



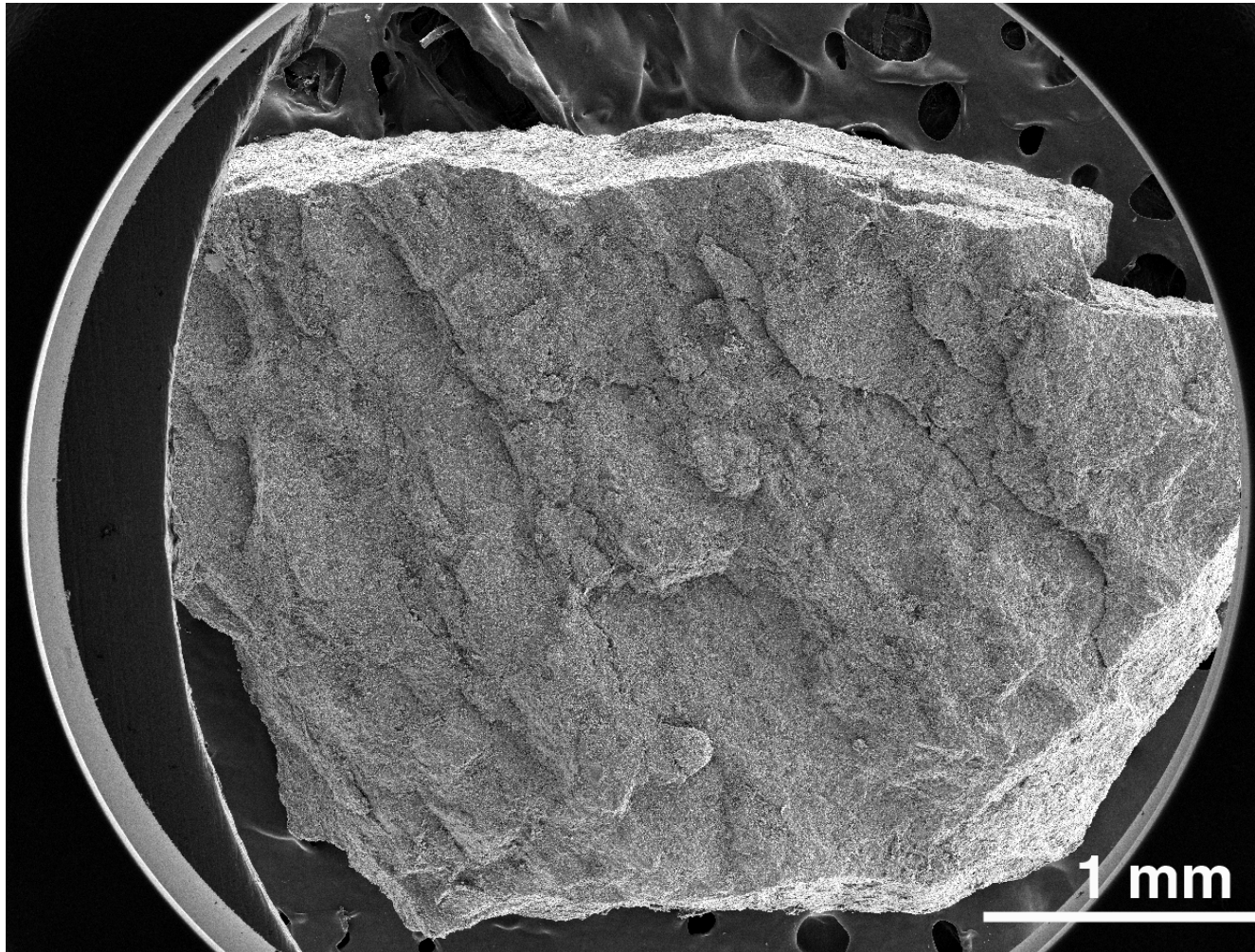
Reconstructed (left) virtual three-  
dimensional solid view and virtual (right)  
damage distribution within the target.



**Micro to nano deformation and damage -  
SEM and TEM Features:  
scale = 10  $\mu\text{m}$  – 1 nm**



# SEM Fractograph of 6 GPa Sample



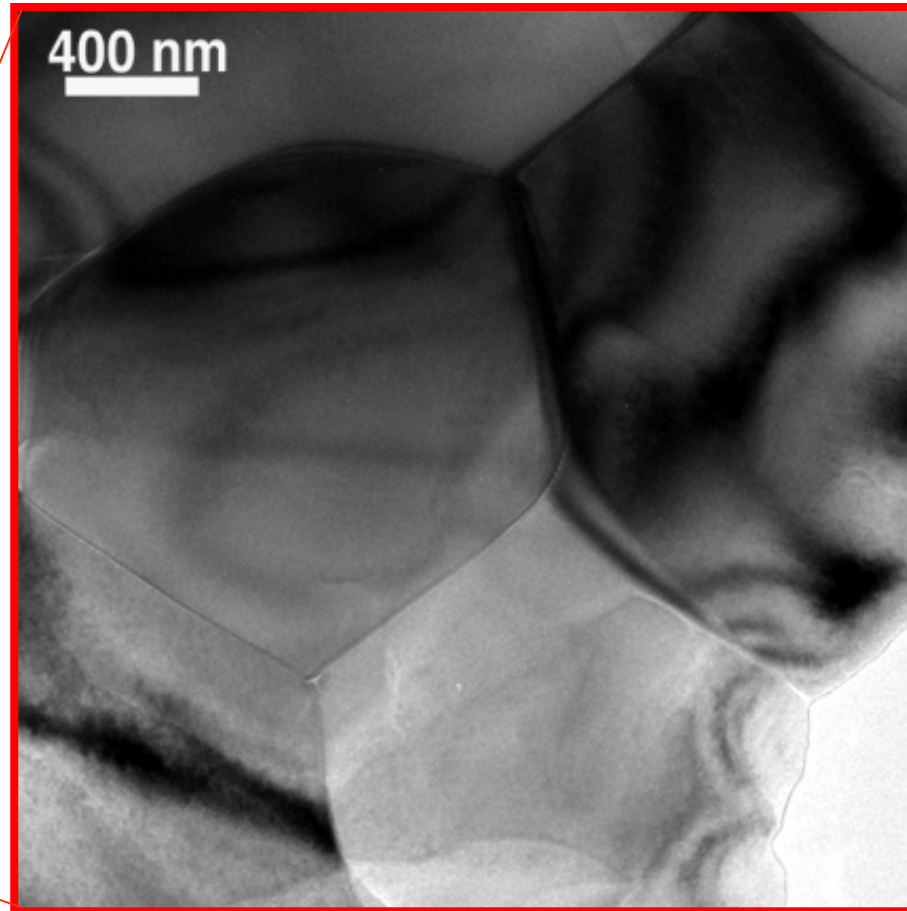
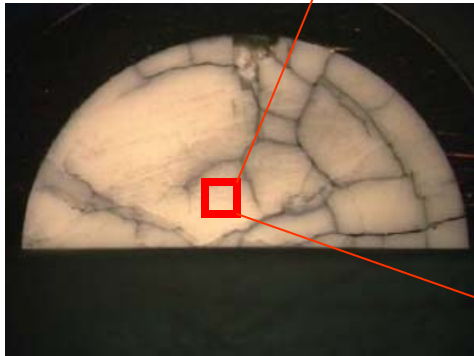
**Fragments obtained by slightly knocking the recovered sample**



# Microstructure of 6 GPa Sample



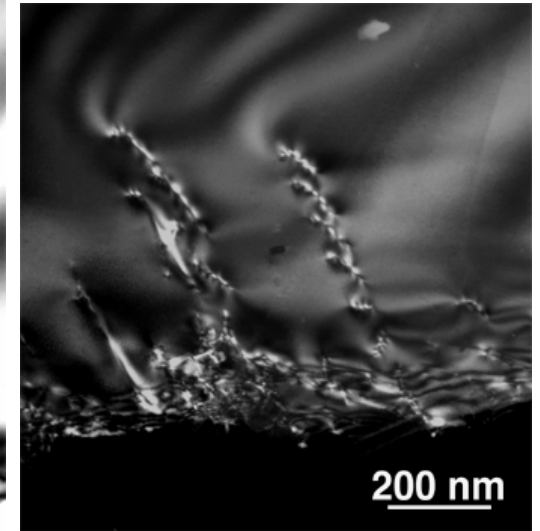
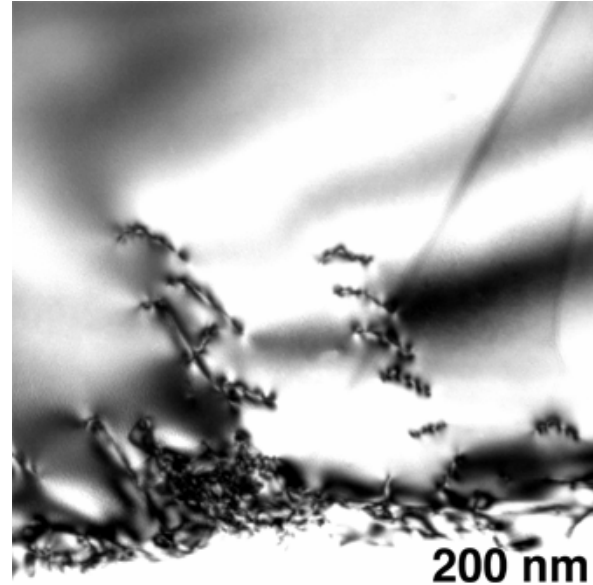
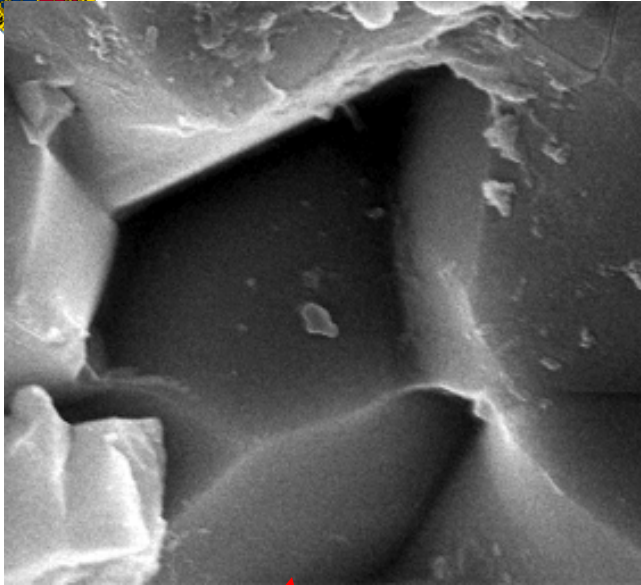
*Area without cracks*



- Crystal defects are rarely observed.
- The size of most grains ranges from 2 to 5  $\mu\text{m}$ .
- No significant voids and secondary phases have been seen.

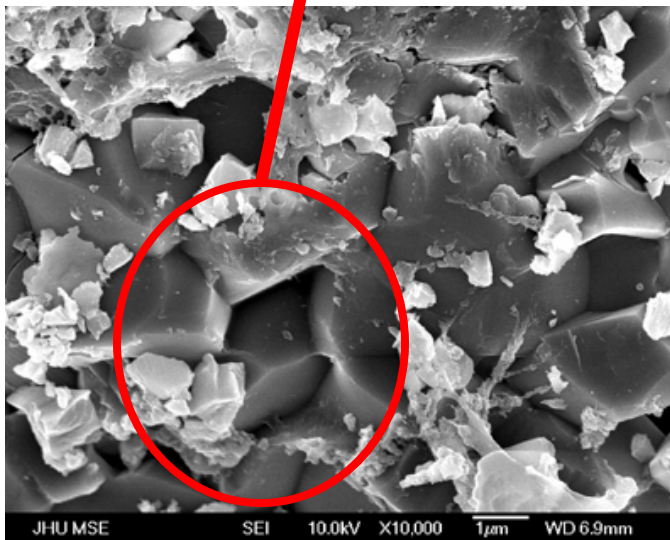


# SEM and TEM of 6 GPA Sample



Bright Field TEM

Dark-Field Image

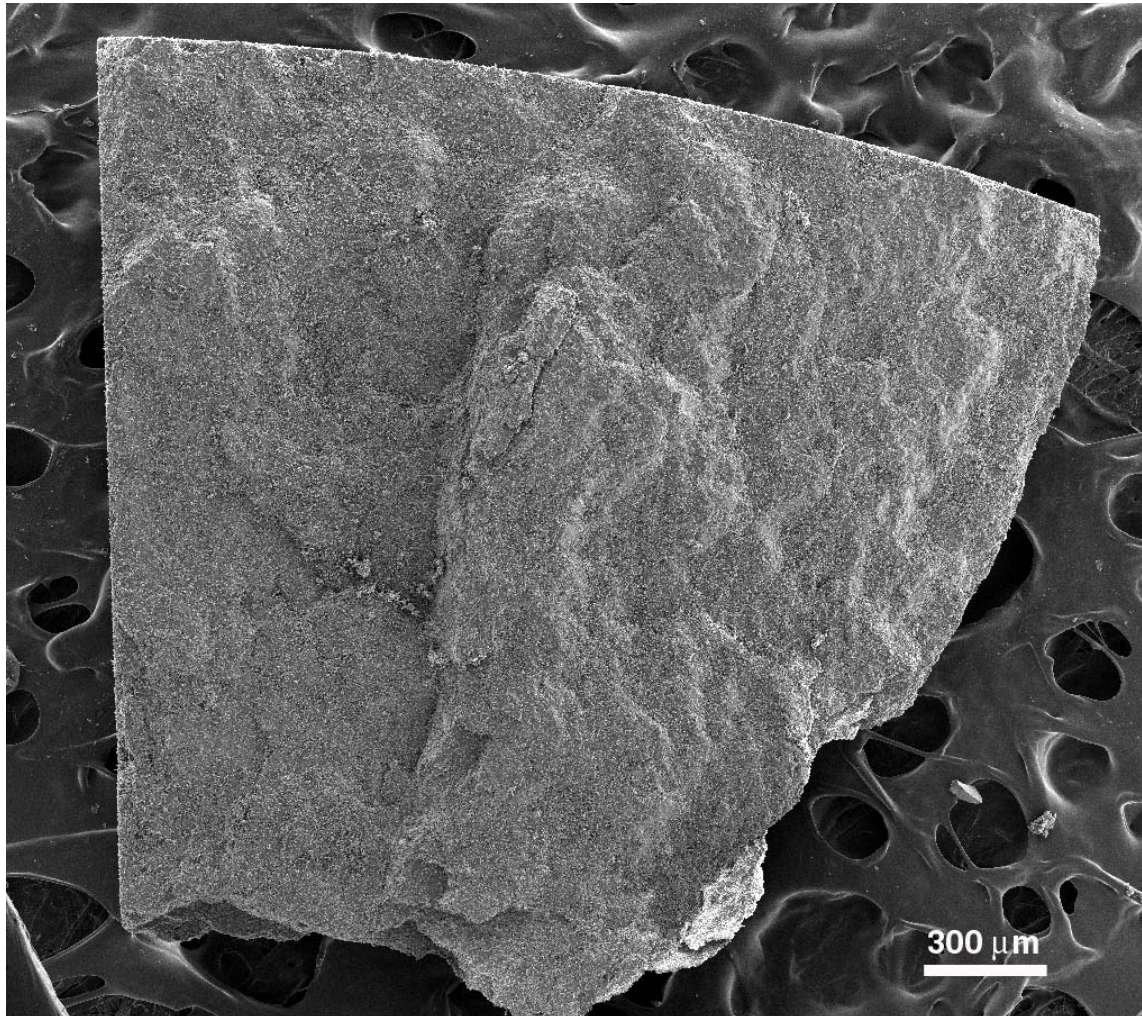


## Conclusions:

- Intergranular fracture seems to dominate
- Dislocation formation at grain boundaries

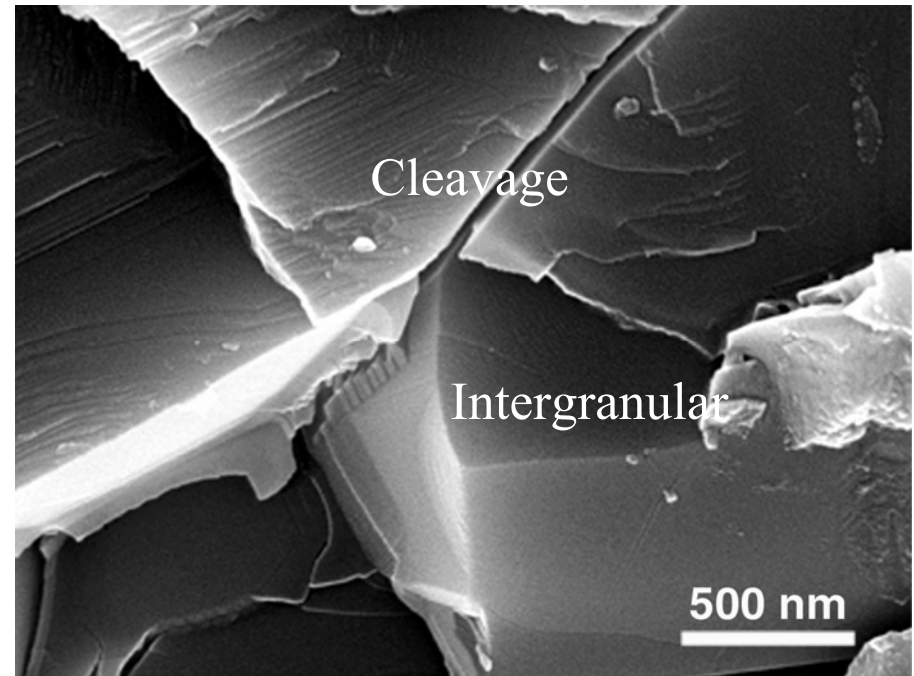
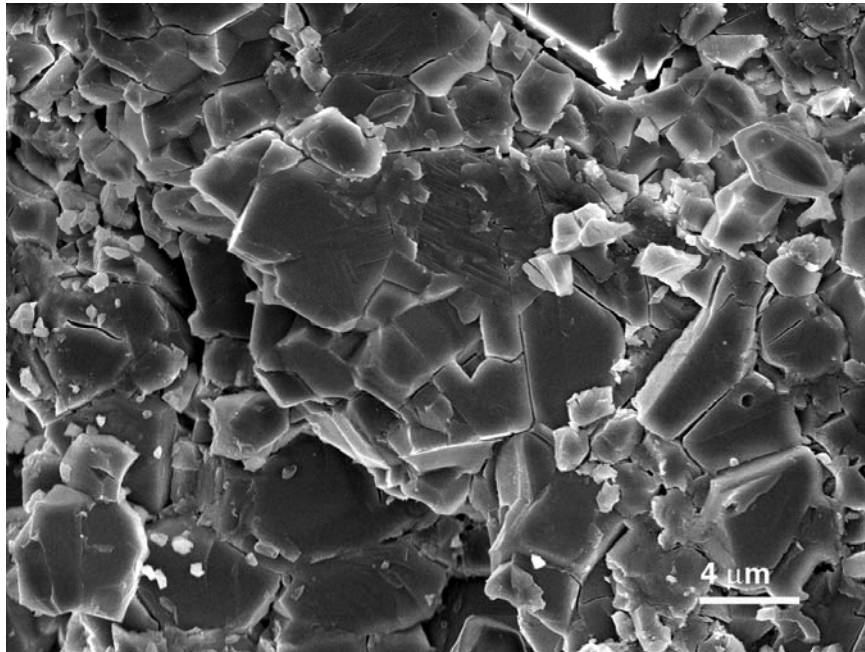


# SEM Fractograph of 7.8 GPa Sample





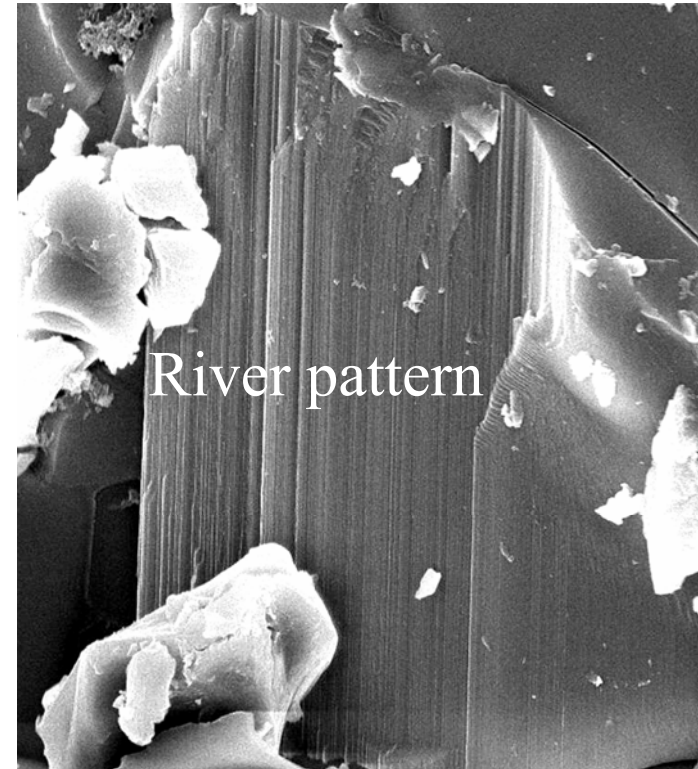
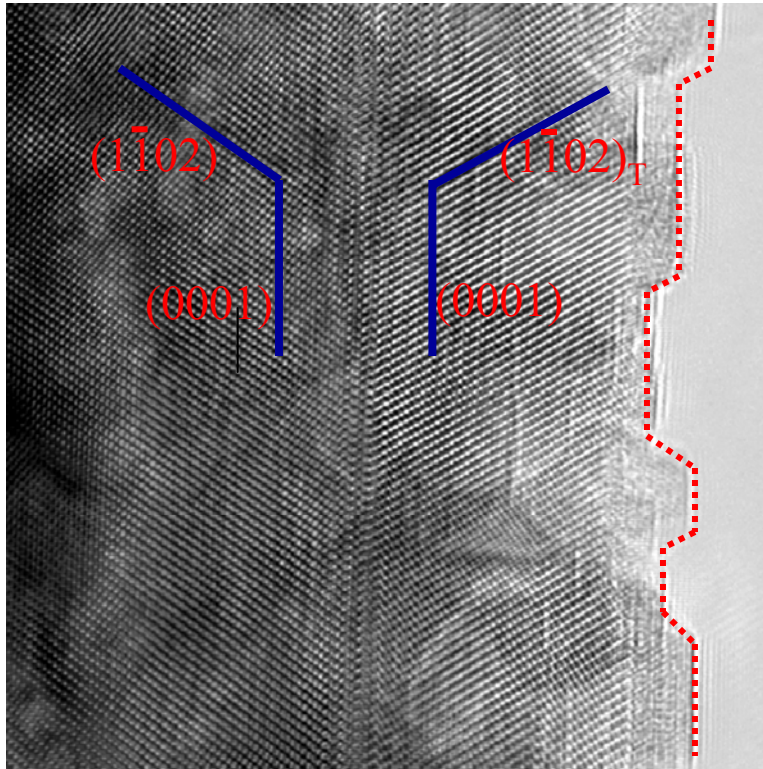
# SEM Fractographs of 7.8 GPa Sample



**Above HEL, fracture is dominated by cleavage**



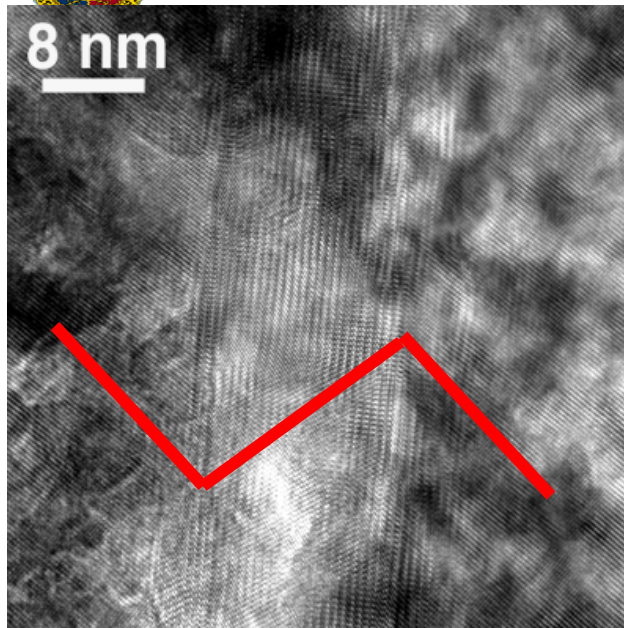
# Deformation Twining vs. Cleavage



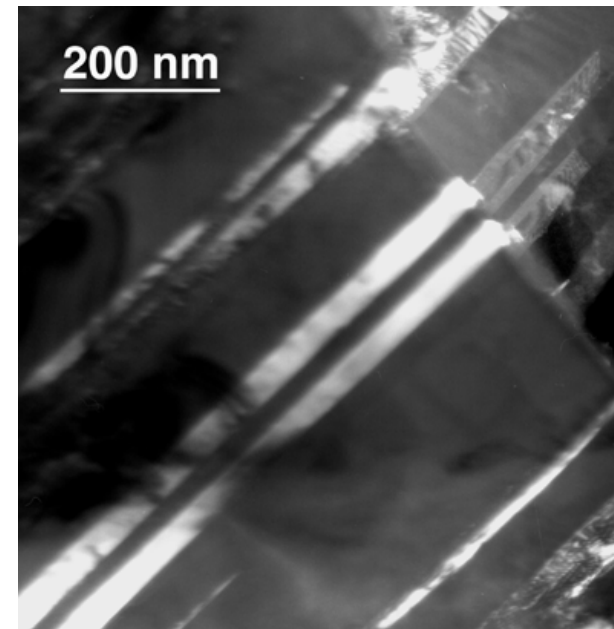
**Fracture facets are mainly parallel to  $(0001)$  and  $(1\bar{1}02)$  planes.**



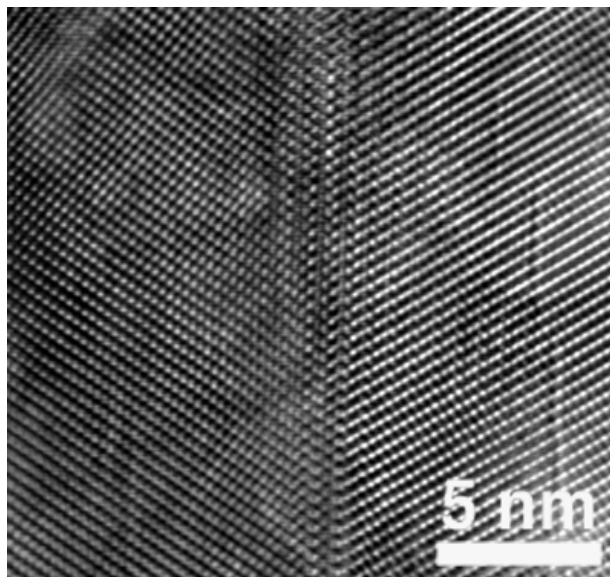
## TEMs of 7.8 GPa Sample



Deformation  
Twinning



Structure of the Twin  
Boundary

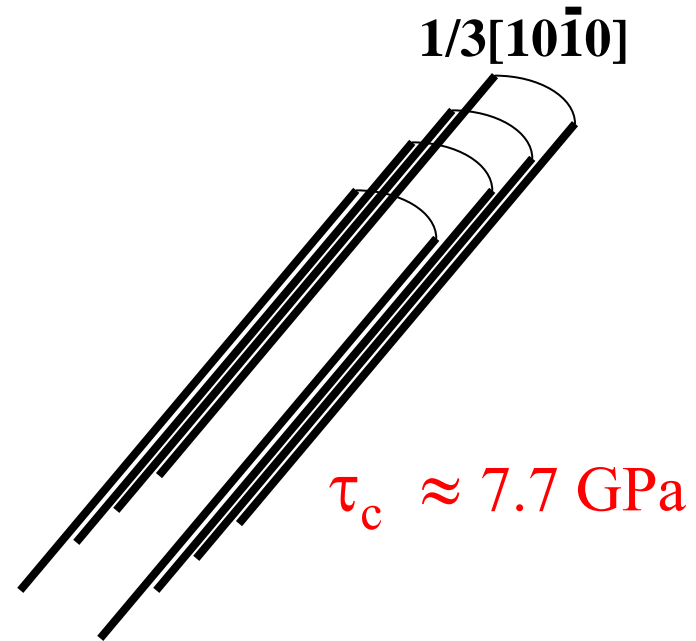
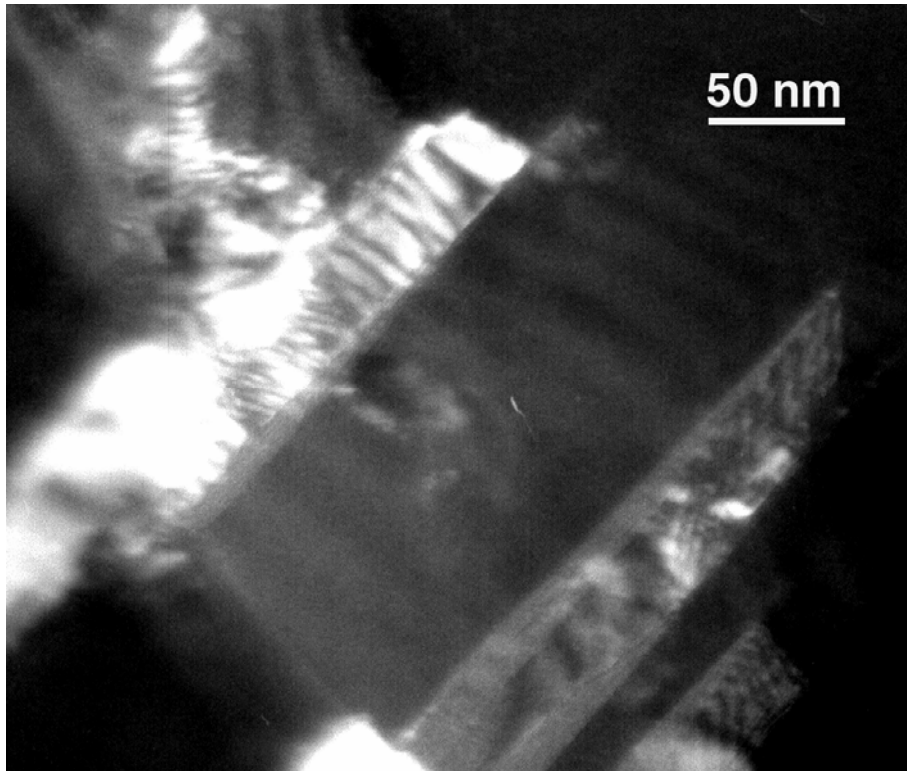


### Conclusions:

- Intragranular cleavage fracture seems to dominate
- Deformation twinning followed by cleavage



# Basal Slip and Twinning of Alumina



Bilde-Sqrensen, et al, *Acta Mater*, 44, 2145 (1996)

*Critical stress to drive partial dislocations to generate stacking fault and deformation twin:*

$$\tau_c = \frac{2\alpha\mu b_p}{D} + \frac{\gamma}{b_p}$$

Chen, et al, Twinning in nanocrystalline aluminum, *Science*, 300, 1275 (2003)

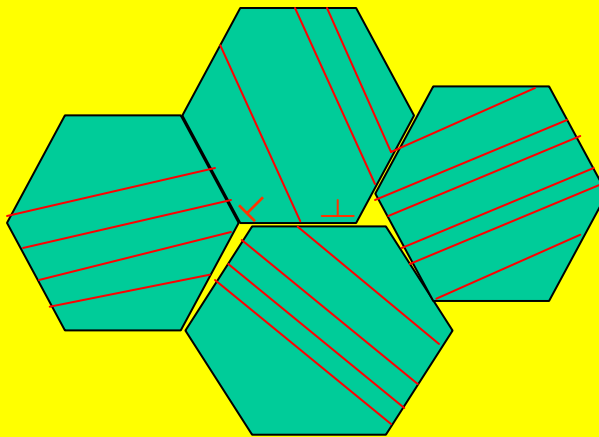
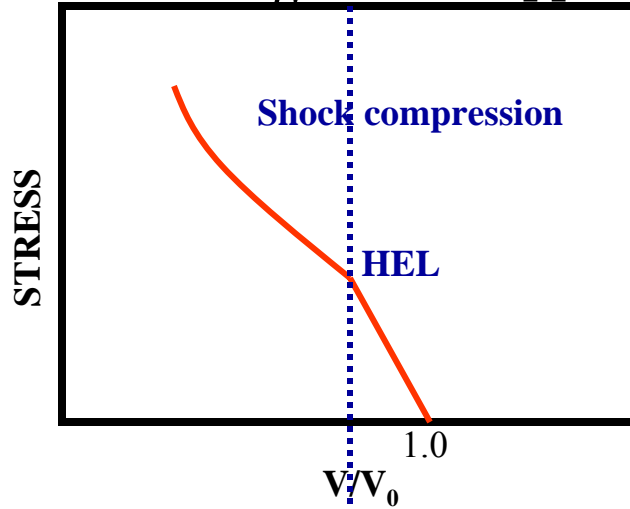
$\tau_c$  is pretty close to the HEL!!! accident? or ...



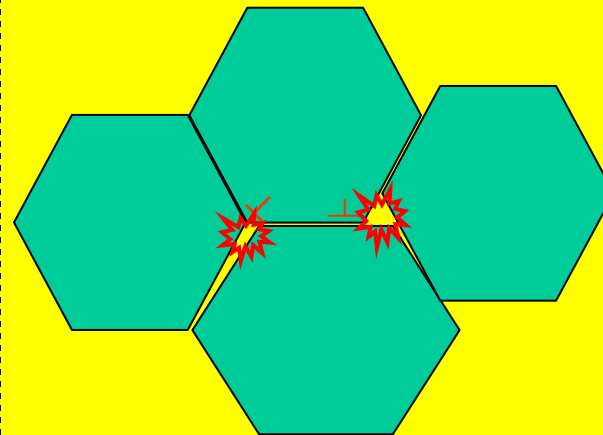
# Deformation/Damage Mechanism Map



$\sigma_{\text{applied}} \geq \sigma_{\text{twinning}}$        $\sigma_{\text{applied}} \geq \sigma_{\text{GB}}$



**Global plastic deformation (twinning) + resultant cleavage**



**Elastic deformation + discontinuous and localized GB cracking**



# Summary and Conclusions



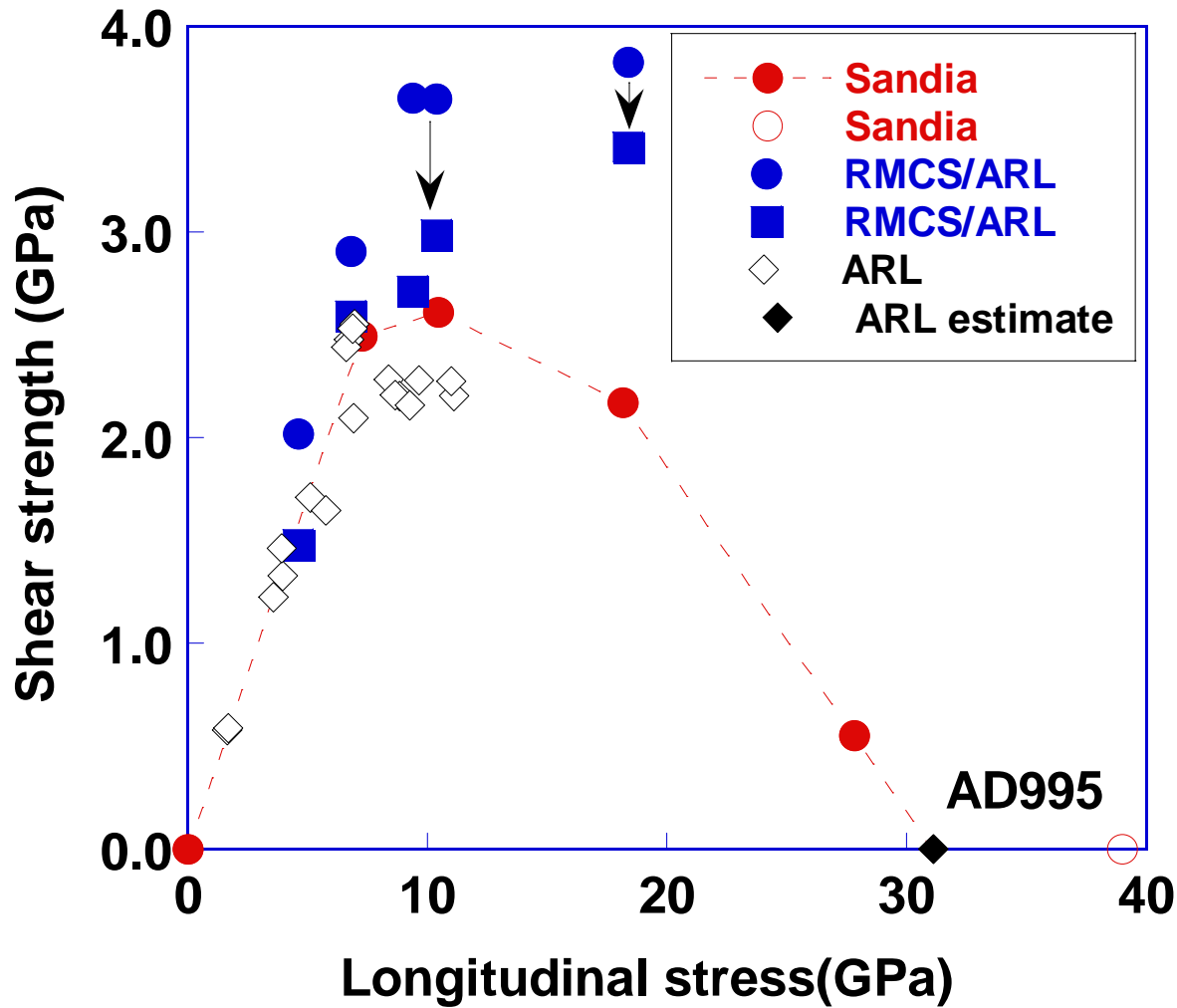
- ❖ Transition from predominantly intergranular to intragranular fracture from below to above HEL.
- ❖ 6 GPa (<HEL) sample:
  - ❖ Crystal defects (twins and dislocations) rarely seen
  - ❖ Dislocations around grain boundaries observed which appear to be produced by accommodation of intergranular cracking
- ❖ 7.8 GPa(>HEL) sample:
  - ❖ Plastic deformation accomplished by twinning widely observed
  - ❖ Twinning planes act as shortcuts for cleavage cracking and is responsible for the transition of fracture mode
- ❖ This work seems to provide strong evidence that the HEL in AD995 is associated with global plastic deformation due to deformational micro-twinning
- ❖ Total length scale spatial deformation and damage identification provides firm experimental basis for validation of ballistic models, computer simulations and performance prediction
- ❖ Deformation and failure mechanism identification at the nano- and micro-scale level will lead to the ability to design ceramics for optimized armor performance – ***“Materials by Design”***



**Thank You For Your Attention**



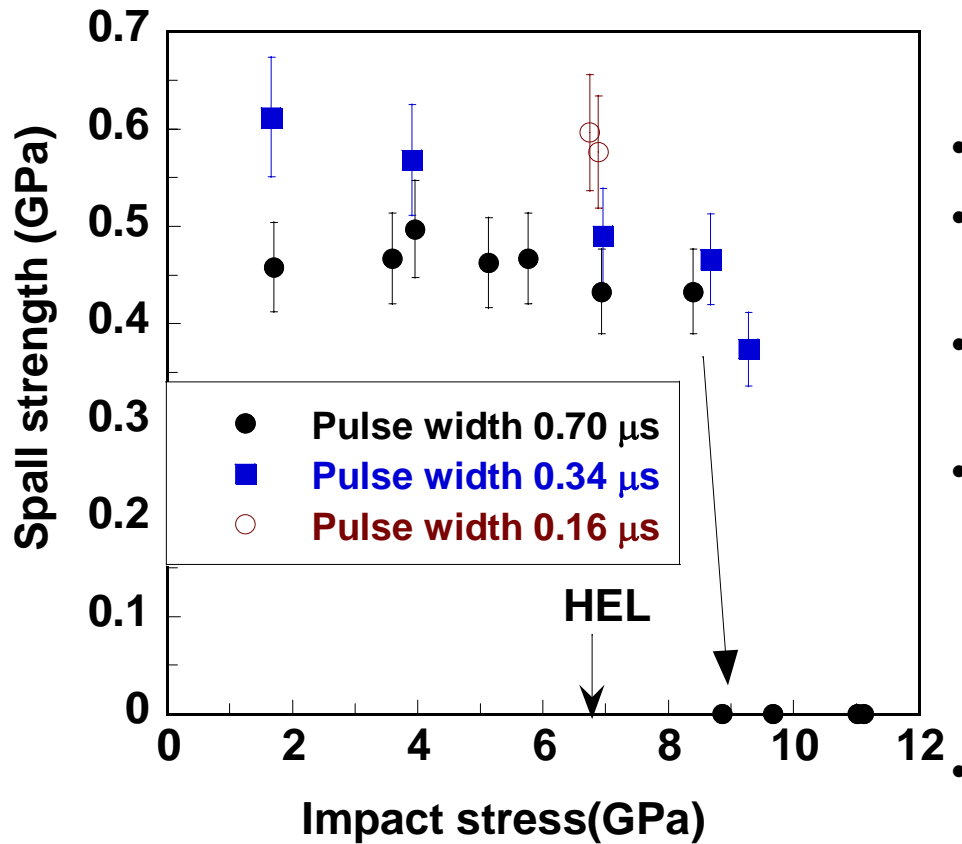
# SHEAR STRENGTH OF AD995



- Increases up to 12 GPa
- Decreases beyond 12 GPa
- Vanishes around 40 GPa.



# SPALL STRENGTH OF AD995



- Compression elastic to 6.7 GPa (HEL).
- Increase in shear strength above the HEL to around 12 GPa.
- Shear strength declines between 12-18 GPa and a total loss above 35 GPa.
- Spall strength dependent on shock compression duration; decreases with an increase in shock induced stress i.e., defects are generated even at less than 6.7 GPa.
- No spall strength above 8.5 GPa i.e., AD995 has no observable cohesion.

Spall strength decreases with both the increasing magnitude of shock and its duration. No measurable spall strength beyond 8.5 GPa.